Chapter 6

GALACTIC COSMIC RADIATION AND SOLAR ENERGETIC PARTICLES

D.F. Smart and M.A. Shea

6.1 NOMENCLATURE AND DEFINITIONS

Energetic charged particle radiation is usually characterized by the energy of the particle in electron volts. An electron volt is the kinetic energy a charged particle gains by being accelerated through a potential difference of one volt. The amount of energy in one electron volt is rather small; particle energies are usually given in units of keV (10^3 eV), MeV (10^6 eV), GeV (10^9 eV), and for extremely high energies, TeV (10^{12} eV). (An electron volt is equal to 1.602×10^{-12} erg.) The total energy of a nucleon E_T is the sum of the kinetic energy E plus rest-mass energy m_oc^2

$$E_T = E + m_oc^2 = mc^2, \tag{6.1}$$

where m_o is the rest mass, m the relativistic mass, and c the speed of light in vacuo. The rest mass energy of a proton m_oc^2 is equal to 938.232 MeV, the rest mass of a neutron is 939.526 MeV, and the rest mass of an electron is equal to 510.984 keV. It is customary in the literature to give values of the kinetic energy per nucleon for heavier particles.

The total energy is related to the particle momentum p by

$$E_T = [p^2c^2 + m_o^2c^4]^{1/2}. \tag{6.2}$$

In the absence of electric fields and of time-varying magnetic fields, E_T and p are constants of the particle's motion.

Observations of the intensity of corpuscular radiation are reported in various units depending upon the detection method. The symbol "J" is normally used to designate the flux, but the precise units must always be specified to avoid ambiguity. There are a number of ways to specify particle flux. The unidirectional differential intensity J(E) is the flux (number per unit time) of particles of a given energy per unit energy interval in a unit solid angle about the direction of observation, incident on a unit area perpendicular to the direction of observation; the units are usually particles $cm^{-2}s^{-1}sr^{-1}$ MeV^{-1}. Unidirectional integral intensity J(>E) is the intensity of particles with energy greater than a threshold energy E

$$J(>E) = \int_E^\infty J(E)dE, \tag{6.3}$$

with units of particles $cm^{-2}s^{-1}sr^{-1}$. Omnidirectional intensities are J(E) or J(>E) integrated over the 4π steradians solid angle, with units of particles $cm^{-2}s^{-1}MeV^{-1}$ or particles $cm^{-2}s^{-1}$ respectively.

A graph of the differential energy spectrum gives J(E) plotted against E; a graph of the integral energy spectrum gives J(>E) plotted against E. The differential energy spectrum J(E) and the integral energy spectrum J(>E) are commonly expressed in two ways, either as a power law in energy,

$$J(E) = J_oE^{-\gamma}, \tag{6.4}$$

$$J(>E) = J_o\frac{E^{-\gamma+1}}{\gamma - 1}, \tag{6.5}$$

where γ is the differential spectral index, or in the exponential form

$$J(E) = J_o \exp\frac{-E}{E_o} \tag{6.6}$$

$$J(>E) = J_oE_o \exp\frac{-E}{E_o} \tag{6.7}$$

where E_o is defined as the characteristic e-folding particle energy, that is, the value over which the flux will fall to 1/e of its previous value. There is a considerable hazard in extrapolating any spectral form beyond the range of the data from which it was derived, and many scientists give the range of values for which specific spectral forms are valid.

When the effects of corpuscular radiation on personnel are of primary concern, particle flux intensities or counting rates must be converted to dose or dose rates. The rad is the unit of absorbed energy; one rad is 100 erg absorbed per gram of absorbing material. A rem (roentgen equivalent man) is the dose absorbed that produces the same biological

effect as one rad of x-rays or γ rays. The relation between the rem and the rad is one rem = rad $\times$ rbe where rbe is the relative biological effectiveness. Conversion of observed particle fluxes to absorbed dose rate, however, is not straight-forward and is sometimes very difficult requiring extremely detailed information on the particle composition and energy spectrum. The conversion depends in a complex way on the energies and kinds of particles and on geometrical configurations of the absorbers and direction of the incident particles, as well as on the different absorbing properties of materials. Computer codes exist [see, for example, Seltzer, 1980] that will convert incident energetic particle fluences into radiation dose behind a specified shield thickness. See Haffner [1967] for a detailed discussion of radiation dosage and the relative sensitivity of various organs to radiation.

The magnetic rigidity P of a particle is a measure of its resistance to a magnetic force that deflects the particle from a straight-line trajectory. The rigidity, with units of momentum per unit charge, is defined as

$$P = \frac{pc}{q}, \tag{6.8}$$

where q is the charge of the particle. If pc is electron volts, then q is the number of electronic charge units and P is in volts. Convenient units are MV (10^6V) and GV (10^9V).

Conversion from rigidity to energy can be accomplished by solving Equation (6.2) for the desired quantity; however, the conversion can be done conveniently by employing the relativistic parameter γ. Conversion from rigidity to energy in terms of kinetic energy per nucleon is

$$E_A = (\gamma - 1)E_{oA} \tag{6.9}$$

where E_A is the kinetic energy per nucleon, and E_{oA} is the rest mass energy per nucleon. Conversion from kinetic energy per nucleon to rigidity is

$$P = \frac{A}{Z}[(\gamma^2 - 1)^{0.5}]E_{oA} \tag{6.10}$$

where A is the atomic number and Z is the atomic charge.

The relativistic parameter γ can be computed from either the cosmic ray kinetic energy or the cosmic ray rigidity.

$$\gamma = \frac{E_A + E_{oA}}{E_{oA}} \tag{6.11a}$$

or

$$\gamma = \left[\left(\frac{PZ}{A/E_{oA}}\right)^2 + 1\right]^{1/2}. \tag{6.11b}$$

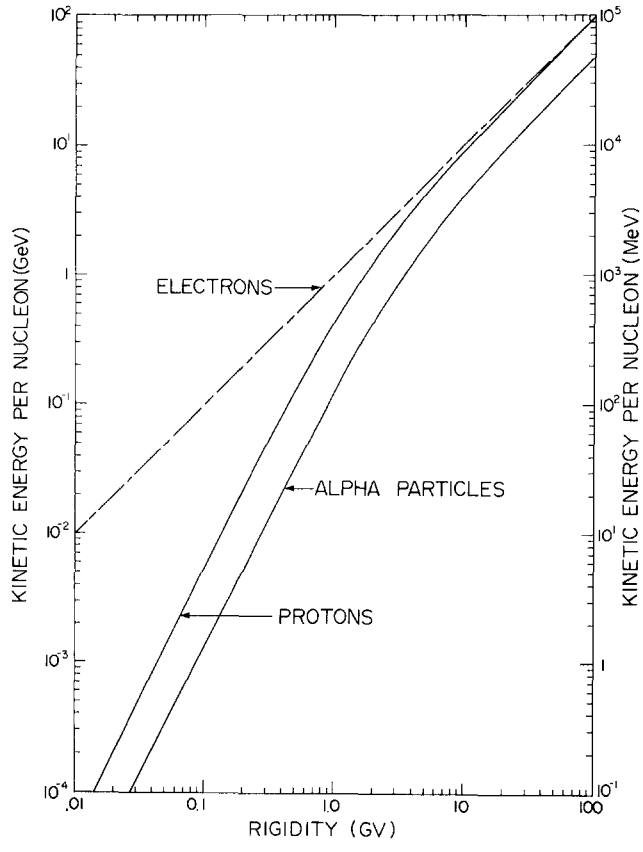

Figure 6-1. Conversion from magnetic rigidity to kinetic energy per nucleon for electrons, protons and alpha particles.

Figure 6-1 shows the relationship between the rigidity of protons, alpha particles, and electrons and their kinetic energy per nucleon. Since most heavy nuclei have an A/Z ratio of approximately two, the alpha particle curve can be used to approximate the rigidity to kinetic energy per nucleon of the heavier nuclei. To obtain the total kinetic energy of a heavy nuclei the energy scale must be multiplied by the total number of nucleons (as an example, by 4 to obtain the total kinetic energy of an alpha particle).

On many occasions the magnetic rigidity is used in place of the kinetic energy in describing the flux spectrum. In particular, in lieu of Equation (6.6), a frequently used expression is

$$J(P) = J_o \exp\frac{-P}{P_o}. \tag{6.12}$$

The earth's magnetic field acts as a momentum analyzer on cosmic rays incident upon the earth's atmosphere. Only those cosmic rays having a momentum per unit charge (that is, rigidity) exceeding that of the threshold of the observation point may be detected at any specified point on the earth's surface or in the earth's magnetosphere. The cutoff or threshold rigidity of cosmic rays is the minimum rigidity that permits

a charged particle to arrive from a specified direction at a given latitude and longitude; particles of lower rigidity are not observed at the specified location and direction because of this geomagnetic cutoff. The geomagnetic field is configured such that particles of progressively lower rigidity are detected as the distance north or south of the equatorial region increases. See Section 6.2.3 for more detailed discussions. More specialized concepts that consider the "bending" of particle trajectories through the magnetic field and allow a mapping of observational directions inside the magnetosphere to directions in interplanetary space are referred to as asymptotic directions and asymptotic cones of acceptance. A more detailed description of these concepts and their use is given by McCracken et al. [1968].

6.2 GALACTIC COSMIC RADIATION

Galactic cosmic radiation is composed of high energy nuclei believed to propagate throughout all space unoccupied by dense matter. Its origin is still a matter of scientific debate and may have both galactic and extragalactic sources. The flux of galactic cosmic radiation is believed to be essentially isotropic outside the heliosphere; propagation effects inside the heliosphere result in an anisotropy of $\sim 1\%$.

Primary cosmic radiation is, by definition, the cosmic radiation incident on the earth's atmosphere. Cosmic rays propagating through the atmosphere undergo nuclear collisions and generate secondary cosmic rays; these secondary cosmic rays consist of all known nuclear and sub-nuclear species.

High energy cosmic ray particles contain a large amount of kinetic energy, and the deposition of this energy can permanently affect the material through which the cosmic ray nucleus passes. In the case of small, state of the art, solid state electronic devices operating in space, the passage of a cosmic ray through a circuit element can generate enough electrons in the sensitive volume to change the state of the circuit element and cause "soft errors" or permanent damage. A recent examination of the effects of cosmic radiation on microelectronics is given by Adams et al. [1981].

6.2.1 Primary Cosmic Radiation

The primary cosmic radiation observed at the earth's orbit consists of approximately 83% protons, 13% alphas, 1% nuclei of atomic number $Z > 2$, and 3% electrons. This composition extends over an energy range from a few hundred MeV to $>10^{20}$ eV. There are no known local planetary sources for the high energy ions observed in the cosmic radiation, but the electron component below about 20 MeV is dominated by Jovian electrons.

The intensity of cosmic rays observed at the earth's orbit is solar cycle dependent undergoing a solar cycle modulation as the inverse of the solar sunspot number cycle. This is discussed more fully in Section 6.2.2.1. The isotropic flux exposure to galactic cosmic radiation in space at sunspot minimum is ~ 4 protons $cm^{-2}s^{-1}$ resulting in a yearly integrated exposure of $\sim 1.3 \times 10^8$ protons/cm^2. The isotropic flux exposure to galactic cosmic radiation at sunspot maximum is ~ 2 protons $cm^{-2}s^{-1}$ resulting in a yearly integrated exposure of $\sim 7 \times 10^7$ protons/cm^2. The galactic cosmic radiation converted to integrated dose results in exposures ranging from 4 rads per year at sunspot maximum to 10 rads per year at sunspot minimum [West et al., 1977].

The differential energy spectra of all high energy cosmic ray nuclei above ~ 1 GeV/nucleon exhibit a spectrum proportional to a power law of the form $dJ/dE \propto E^{-\gamma}$, where E is the kinetic energy per nucleon and γ is the spectral index. Below ~ 1 GeV/nucleon, the differential spectrum of cosmic ray nuclei observed at the earth's orbit deviates from a simple power law. The differential spectrum becomes flatter with decreasing energy until a maximum in the differential intensity is reached around a few hundred MeV/nucleon. Below the maximum, the differential intensity decreases monotonically to a few tens of MeV/nucleon. The primary cosmic radiation spectrum observed for protons and alpha particles in the inner heliosphere around the earth's orbit is shown in Figure 6-2. At the vicinity of the earth, the low energy portion of the spectrum changes with time. These changes are mainly the effects of solar modulation, and are illustrated by the shaded and hatched areas of Figure 6-2.

6.2.1.1 Elemental Composition of Primary Cosmic Radiation. Nuclei heavier than helium comprise only about 1% of the total primary cosmic radiation and have a total integral intensity of about 25 particles $m^{-2}s^{-1}sr^{-1}$. Cosmic ray nuclei with $Z > 2$ are classified into various charge groups such as light (L), medium (M), light-heavy (LH), and very heavy (VH). The L-group nuclei include those with $3 < Z \leq 5$, the M-group with $6 \leq Z \leq 8$, the LH-group with $9 \leq Z \leq 14$, the H-group with $15 \leq Z \leq 19$ and the VH-group with $20 \leq Z \leq 28$. The charge group from manganese ($Z=25$) to nickel ($Z=28$) is commonly referred to as the iron group.

During their travel from the source regions to the vicinity of the earth, the cosmic rays interact with the interstellar medium, and some fragmentation occurs resulting in a depletion of the heavy charged primary cosmic rays and an increase of the lighter nuclei compared to the "Universal Abundance" shown in Figure 6-3. The relative abundance of the various nuclei observed at the earth for energies greater than 0.45 GeV/nucleon are shown in Table 6-1 [Lezniak and Webber, 1978].

The abundance of the elements N, Na, Al, S, Ar, Ca, Cr, and Mn is enhanced in the cosmic radiation observed in the heliosphere as a result of fragmentation in the intersellar medium. Almost all of the abundance of the elements Li, Be, B, F, Cl, K, Si, Ti, and V is due to fragmentation of heavier cosmic

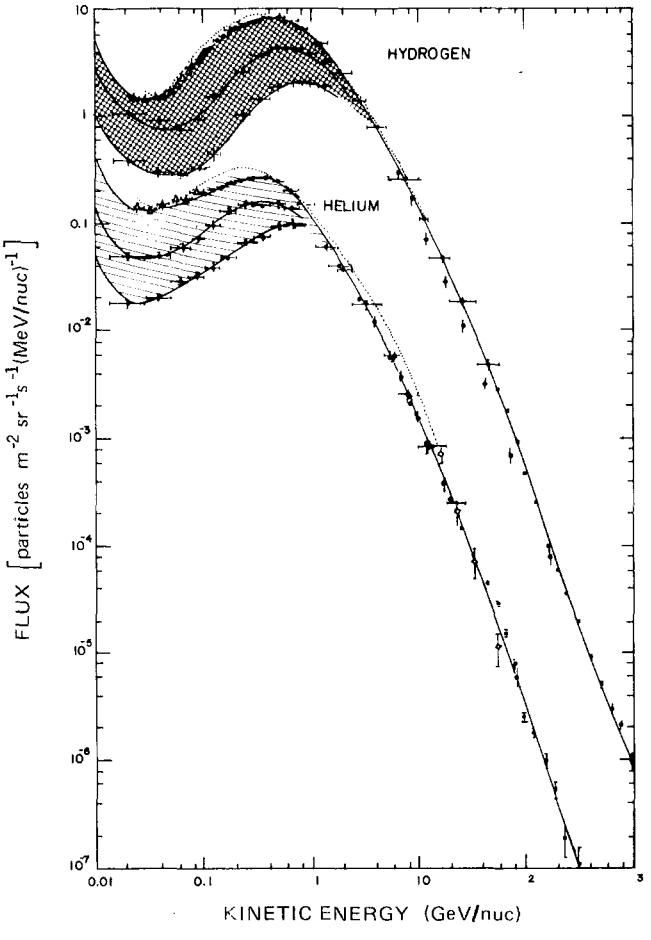

Figure 6-2. Primary cosmic ray differential energy spectrum. The upper envelope indicates the solar minimum spectrum while the lower envelope indicates the solar maximum spectrum. The shaded area indicates the range of the solar modulation over a solar cycle. The hydrogen spectrum in this figure has been multiplied by a factor of 5 so the modulated portion of the spectrum avoids merging with the top of the helium spectrum.

ray nuclei (that is, higher charge number elements) during their propagation through the interstellar medium. The ratios of the cosmic ray elemental abundance to the solar system elemental abundances are generally ordered by atomic parameters such as the first ionization potential, at least up through Z = 40 (as shown in Figure 6-4), with exceptions to this rule at H, He, C, N, and possibly Ne and Mo.

6.2.1.2 The Anomalous Cosmic Ray Component. The low energy portion of the cosmic ray spectrum is quite variable reflecting its dependance on solar modulation. In 1972, during the decline of the 20th solar sunspot cycle, anomalies in the energy spectra and composition were noted at energies ≤70 MeV/nucleon. These differences persisted through sunspot minimum and continued throughout the rising portion of the 21st solar sunspot cycle but seem to have disappeared after the maximum of the 21st solar cycle. This behavior leads to the suggestion that the anomalous

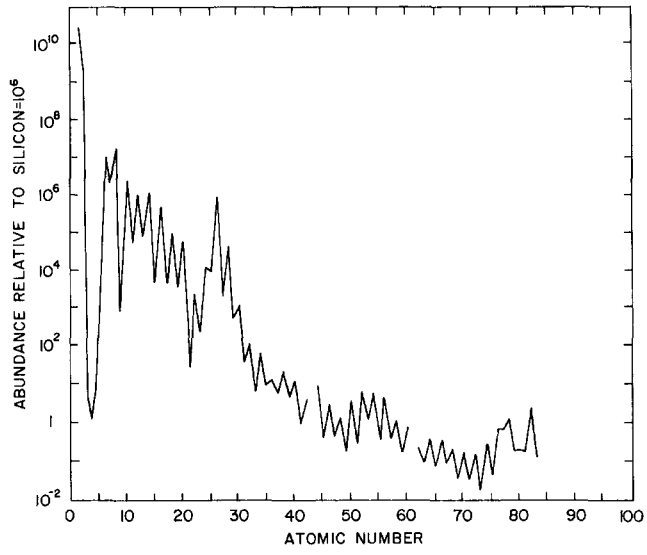

Figure 6-3. The universal abundance of the chemical elements in nature relative to silicon = 10^6. These results were obtained from studies of meteorites, our sun and other stars. [Data from Cameron, 1981.]

Table 6-1. Cosmic-ray composition as observed at 1 AU.

Charge	>450 MeV/Nuc
He	44700 ± 500
Li	192 ± 4
Be	94 ± 2.5
B	329 ± 5
C	1130 ± 12
N	278 ± 5
O	1000
F	24 ± 1.5
Ne	158 ± 3
Na	29 ± 1.5
Mg	203 ± 3
Al	36 ± 1.5
Si	141 ± 3
P	7.5 ± 0.6
S	34 ± 1.5
Cl	9.0 ± 0.6
A	14.2 ± 0.9
K	10.1 ± 0.7
Ca	26 ± 1.3
Sc	6.3 ± 0.6
Ti	14.4 ± 0.9
V	9.5 ± 0.7
Cr	15.1 ± 0.9
Mn	11.6 ± 1.0
Fe	103 ± 2.5
Ni	5.6 ± 0.6

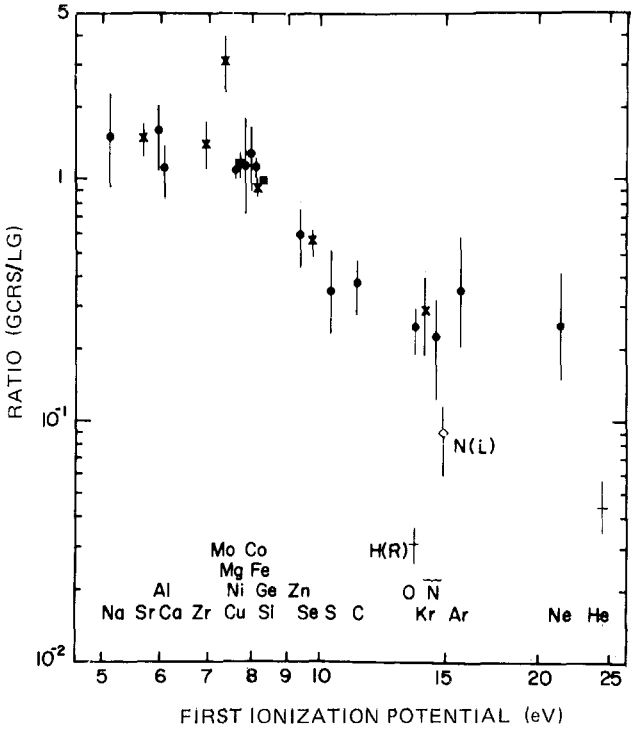

Figure 6-4. Ratio of the galactic cosmic ray source (GCRS) to the "local galactic" (LG) elemental abundances at 1 AU ordered by the first ionization potential [after Mewaldt, 1981].

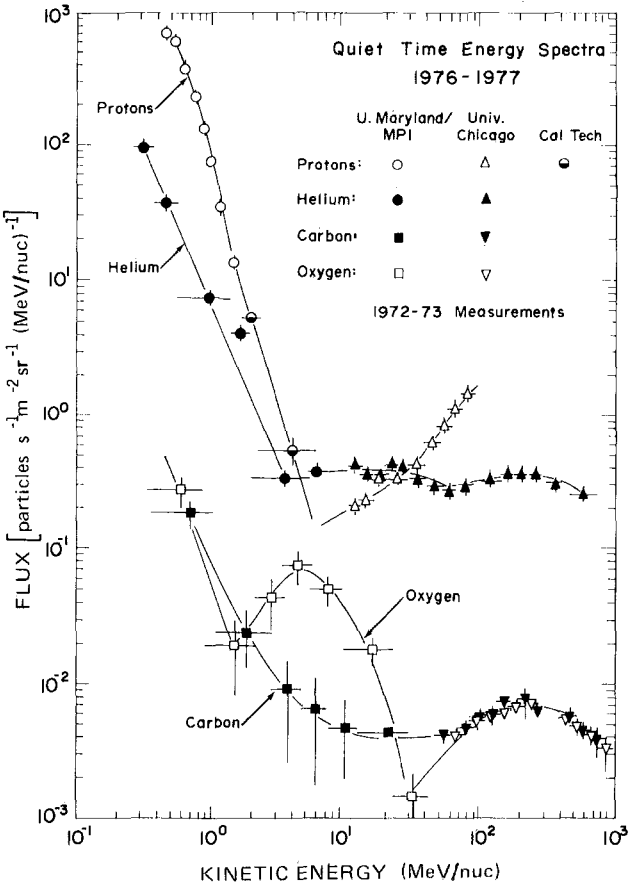

Figure 6-5. The "anomalous" cosmic ray spectrum. The differential energy spectra of hydrogen, helium, carbon,and oxygen observed in the interplanetary medium near 1 AU during the solar minimum in 1976–1977 during quiet-times. The "anomalous cosmic ray" component appears between ~2 and ~30 MeV/nucleon and is characterized by large overabundance of He and O compared to H and C,respectively [Gloeckler, 1979].

component may be solar magnetic cycle dependent and only present during alternate cycles. The anomalous component resulted in the low energy cosmic ray spectra shown in Figure 6-5. The "anomaly" can be seen by comparing this spectra with that of the previous solar minima, the upper envelope of the low energy portion of the spectra shown in Figure 6-2. In a review of this anomalous component, Gloeckler [1979] noted that the helium spectra above ~ 2 MeV/nucleon was relatively flat, and between ~ 5 and 30 MeV/nucleon He was more abundant than protons. The oxygen spectrum possessed an unusual hump between ~ 2 and 20 MeV/nucleon with no comparable feature for carbon, and at ~ 5 MeV/nucleon oxygen was some 10 to 20 times more abundant than carbon. In addition to helium and oxygen, nitrogen and neon were observed to be more abundant in the anomalous component than in the ≥100 MeV/nucleon galactic cosmic rays. The abundances relative to carbon of the major elements in the anomalous component are compared to the composition of galactic cosmic rays in Table 6-2. Assuming that 2–30 MeV/nucleon carbon is of predominately galactic origin during quiet times, the elements He, N, O, Ne, and possibly Fe were from 5 to 20 times more abundant in the anomalous component than in the normal cosmic ray composition. Within statistical uncertainties the composition of the other elements in the anomalous component region were comparable to that expected from the galactic cosmic ray flux.

Table 6-2. Abundances relative to carbon of the anomalous component and galactic cosmic rays.

Element	Anomalous Component (2-30 MeV/nucleon)[(a)]	Galactic Cosmic Rays (>100 MeV/nucleon)
H	40 ± 4	275
He	90 ± 10	50
C	≡ 1	≡ 1
N	3 ± 1	0.225
O	18 ± 4	1.0
Ne	1.3 ± 0.4	0.175
Mg	0.3 ± 0.2	0.23
Si	$0.2^{+0.25}_{-0.15}$	0.17
Fe	0.6 ± 0.2	0.12

(a) Approximate energy range of the measurements in MeV/nucleon.

6.2.1.3 Cosmic Ray Electrons. The interplanetary cosmic ray energetic electrons of non-solar origin measured at 1 AU has two components, a galactic cosmic ray electron component and a Jovian electron component. All electron flux in the heliosphere below about 25 MeV are of Jovian origin [Eraker and Simpson, 1981]. At the earth's orbit, for energies greater than ~ 100 MeV, the galactic cosmic ray electron flux dominates. A composite primary electron spectrum is shown in Figure 6-6. The solar cycle modulation dominates the variability in the electron spectrum from about 100 MeV to about 5 GeV.

Jupiter's magnetosphere is a source of relativistic electrons that can be observed throughout the entire heliosphere. Within several AU of the planet Jupiter, the flux is modulated with the characteristic 10-hour planetary rotation period. The MeV Jovian electron flux observed at the earth has a 13-month "seasonal" characteristic. This "seasonal" effect results from the relative position of Earth and Jupiter as the planets revolve around the sun in their respective orbits. When the interplanetary magnetic field lines passing near the earth connect to the Jovian magnetosphere (the Jovian magnetosphere being a minimum of 5 AU in length), the propagation of the Jovian electrons from Jupiter to the earth is more efficient. However, the propagation characteristics are still quite variable, depending on the status of the interplanetary medium. The most favorable connection of the interplanetary magnetic field lines between the earth and Jupiter repeats at approximate 13-month intervals with corresponding peaks in the electron flux during the "electron season" which may last for several months. Before the presence of the Jovian electrons was established, these "quiet time electron increases" were unexplained.

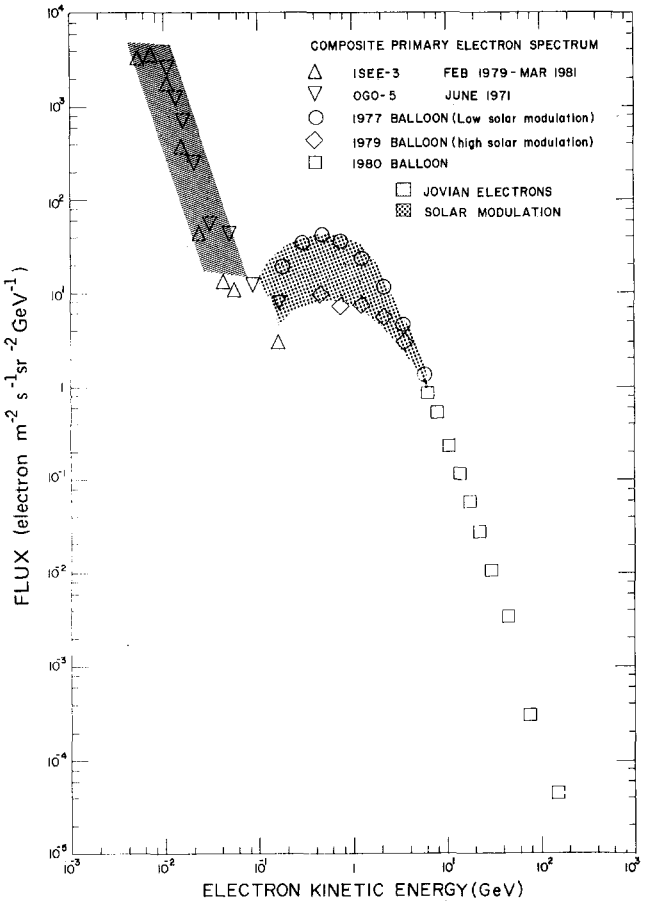

Figure 6-6. Composite primary cosmic-ray electron differential energy spectrum [courtesy P. Meyer, University of Chicago, Private Communication].

6.2.2 Cosmic Ray Flux Modulations

Cosmic ray flux modulations can be divided into three groups. The long term modulation (millions of years), solar cycle modulations (usually referred to as the 11-yr cycle), short term modulations (consisting of cyclic variations ranging from a semi-diurnal variation to a 27-day variation, and transient variations consisting of decreases and increases associated with various solar phenomena).

There is conjecture about variations in the galactic cosmic ray sources over very long time scales. The analysis of cosmic ray exposure to meteorites and lunar rocks is both limited and complicated. So far, statistics and uncertainty in the determinations only allow the conclusion that the current cosmic ray composition has not changed by more than a factor of two over the last 10^8 years. The isotopic composition of the cosmic radiation, specifically the ^{10}Be isotope presumed to be a spallation product of cosmic ray interaction in the interstellar medium, results in a probable cosmic ray age of ~ 15–17 million years.

Cosmogenic isotopes produced by the cosmic ray interactions in air, such as ^{26}Al, ^{10}Be, and ^{14}C, and then frozen in sea sediments, ices or biological materials produce somewhat better limits on possible cosmic ray variations. The ^{10}Be isotope sediments over the last two million years show less than a 30% variation in the cosmic radiation.

The carbon-14 variations are most likely due to the strength of the solar modulation effect. These variations of a few percent have the amplitude and phase expected from historical and recent sunspot data, cosmic ray modulation observations, and CO_2 transport theory [Forman and Schaffer, 1979].

6.2.2.1 Solar Cycle Modulations. The galactic cosmic radiation exhibits an intensity variation with ~ 11-yr periodicity, as shown in Figure 6-7. The cosmic ray intensity changes at the earth are inversely correlated with the sunspot number and lag changes in sunspot number by 9 to 12 months. The increase in solar activity modulates the galactic cosmic rays, through the agency of the solar wind, in such a manner that an increase in solar activity corresponds to a decrease in the cosmic ray intensity. From solar cycle minimum to solar cycle maximum, the energy density of the primary galactic cosmic rays in the vicinity of the earth decreases by about 40%. The cosmic ray intensity, as ob-

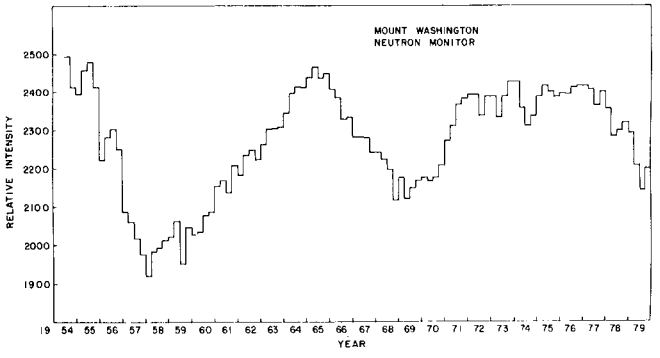

Figure 6-7. Illustration of the ~ 11-yr solar cycle modulation of galactic cosmic rays observed at the earth by the Mt. Washington neutron monitor from 1954 thru 1979.

served at the earth, does not change smoothly from maximum to minimum values. It decreases by a series of sharp drops followed by partial recovery until the minimum intensity is reached near the maximum in solar activity. The recovery to maximum cosmic ray intensities may be either a slow rise, as observed from 1958–1964, or a rapid increase as observed from 1970–1972. These two variations in increasing cosmic ray intensity are also observed in the ionization chamber records going back to 1933, giving rise to a 22-yr solar cycle variation. The historical record of sunspot observations shows longer (80–200 yr) periods modulating the amplitude of the sunspot number cycle. The variations in the carbon-14 record seem to correlate with these same periods. See, for example, Stuiver and Quay [1980].

Theory of Solar Cycle Modulation. There has been considerable theoretical work attempting to model the modulation of cosmic rays by the interplanetary medium. The physical model is based on a solar system filled with an expanding fully ionized and highly conducting plasma, the solar wind (see Chapter 3), which contains frozen-in irregular magnetic fields. Cosmic rays undergo many scatterings from these irregularities and execute a random walk in the solar wind. The cosmic ray population outside the heliosphere diffuses inward, and during this diffusive process it undergoes deceleration by the adiabatic cooling associated with the expansion of the solar wind. The parameters required to define the transport equation and its solution are the diffusion coefficient (generally a function of radius and energy), the solar wind velocity, and the interstellar energy spectrum.

The basis of current solar modulation theory is the Fokker-Planck equation for the modulated number density U(r,E) per unit kinetic energy at heliocentric radius r and kinetic energy E. Gleeson and Axford [1967, 1968] have given this equation as

$$\frac{1}{r^2}\frac{\partial}{\partial r}(r^2VU) - \frac{1}{3r^2}\frac{\partial}{\partial E}(r^2V)\frac{\partial}{\partial E}(\alpha EU) - \frac{1}{r^2}\frac{\partial}{\partial r}\left(r^2K\frac{\partial V}{\partial r}\right) = 0 \quad (6.13)$$

where V is the solar wind velocity and K the effective diffusion coefficient in the interplanetary magnetic field irregularities. The diffusion coefficient is generally a function of $\beta = (v/c)$, magnetic rigidity and radial distance. The factor $\alpha = (\gamma + 1)/\gamma$, where γ is the relativistic factor. Numerical techniques for solving Equation (6.13) have been developed by cosmic ray modulation theory specialists. These techniques require the specification of the interstellar density spectrum $U(E_o)$, the functional form of the diffusion coefficient, and appropriate boundary conditions. Numerical solutions of equation (6.13) yield the modulated spectra at 1 AU.

The solar cycle modulation of the cosmic ray spectra is described quantitatively by the "modulation parameter," ϕ. This parameter is defined as

$$\phi = \int_r^{R_1} \frac{V}{3K_1(r)}dr \quad (6.14)$$

where V is the solar wind velocity and $K_1(r)$ is the radial part of the diffusion coefficient. The diffusion coefficient K is usually treated as a separable function of radius and rigidity. In practice the actual value of the cosmic ray modulation parameter at a specific instant of time is difficult to determine. A reference level (such as the counting rate of a stable neutron monitor) is correlated with the historically derived modulation parameters as shown in Figure 6-8, and

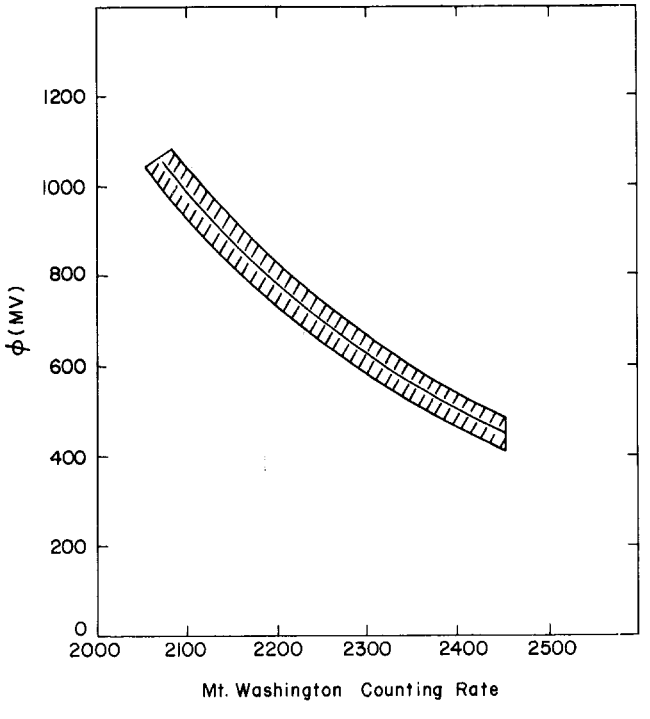

Figure 6-8. Correlation between the cosmic ray modulation parameter ϕ and the counting rate of the Mt. Washington neutron monitor.

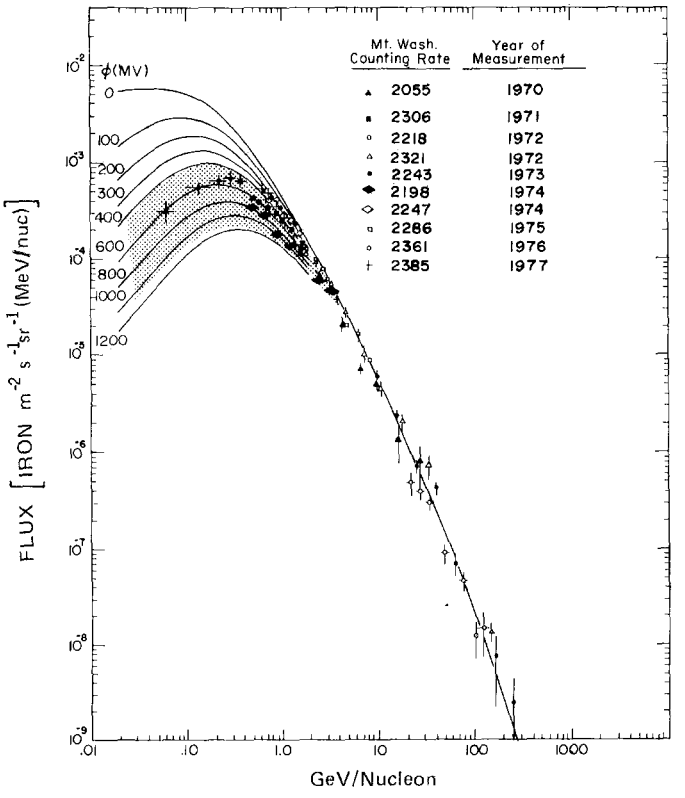

Figure 6-9. Differential energy spectra for cosmic-ray iron nuclei. The shaded area indicates the range of the solar cycle modulation.

the current neutron monitor counting rate is used as a reference modulation level.

Solutions of Equation (6.13) result in an analytic description of the cosmic ray spectrum as a function of kinetic energy and solar modulation parameter.

$$J(E,\phi) = A\frac{[E(E + 2E_{oA})(E + \phi + M)^{-\gamma}]}{[(E + \phi)(E + 2E_{oA} + \phi)]}, \quad (6.15)$$

where E is the kinetic energy of the cosmic ray nuclei in MeV/nucleon, E_{oA} is the rest mass energy of the cosmic ray nuclei in MeV/nucleon and ϕ is the modulation parameter. To model the cosmic ray proton spectrum Garcia-Munoz et al. [1975] present solutions of the cosmic ray spectrum for various modulation levels and elements of the cosmic ray flux. Figure 6-9 shows modulated differential iron spectra for various values of the modulation parameter ϕ. The shaded areas indicate the range of the modulation observed during the past few solar cycles.

6.2.2.2 Short Term Modulations. Short term modulations can be subdivided into two types, cyclic variations and transient variations.

Cyclic Variations. There are ~ 27-day variations in the observed cosmic ray intensity within the heliosphere, at least in the regions explored from 0.3 to 20 AU. These variations are statistical averages associated with the structure of the interplanetary medium corotating with the sun. The amplitude of these variations, as observed by ground-level neutron monitors, is quite variable, normally a few percent, ranging from about 1% to 5%.

For cosmic ray detectors located on the earth there are also diurnal and semi-diurnal variations in phase with the earth's rotation. The amplitude of these diurnal variations is variable ranging from a maximum of a few percent to a minimum of about 0.1%. Figure 6-10 shows an enhanced daily variation continuing for several days. During stable interplanetary conditions the maximum amplitude occurs at ~ 1800 h local solar time. This corresponds to an asymptotic direction roughly along the direction of the sun-earth Archimedean spiral path continuing outward from the earth into interplanetary space.

The semi-diurnal variation is usually less than 0.1% and maximizes in both directions along a line 135° west of the earth-sun line, a direction perpendicular to the mean interplanetary magnetic field direction at the orbit of the earth.

The presence of a sidereal variation reflecting a galactic anisotropy is still not firmly established, and if present would have an extremely small amplitude of a few hundredths of a percent.

Transient Variations. There can be both sudden decreases, and more rarely, increases in the cosmic radiation flux that result from solar activity. Sudden decreases in intensity, called Forbush decreases (named after the original discoverer) are associated with sudden increases in the plasma density and magnetic flux emitted from the sun. The large Forbush decrease events are generally associated with "large"

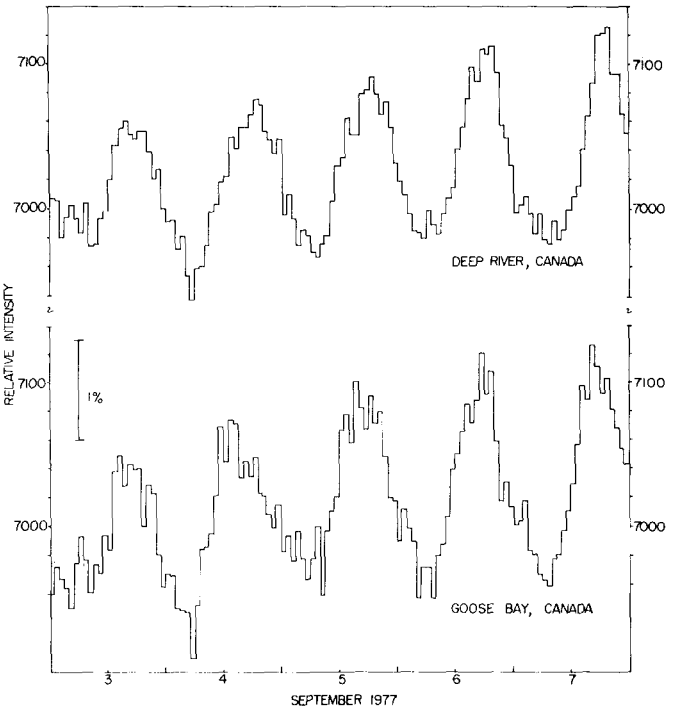

Figure 6-10. Illustration of an enhanced cosmic ray daily variation.

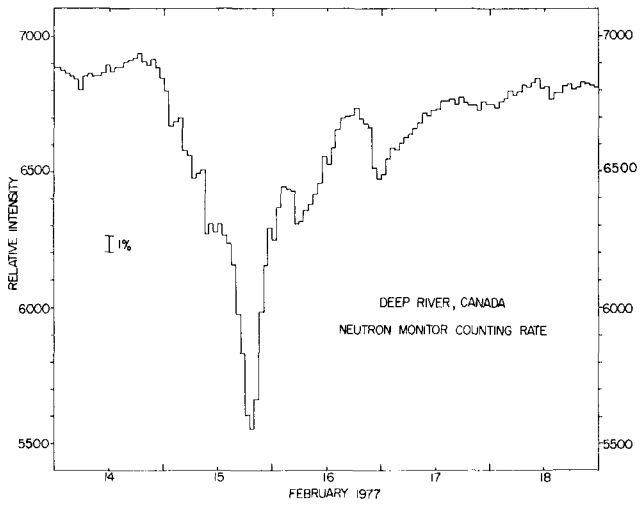

Figure 6-11. Illustration of a cosmic ray Forbush decrease.

solar flares and interplanetary shock structures. The magnitude of these decreases is quite variable ranging from a few percent to as great as 35% in the most extreme case yet recorded by neutron monitors on the earth. An example of a Forbush decrease is shown in Figure 6-11.

There are two types of "cosmic ray" increases attributable to the sun. The solar "cosmic ray" event is discussed in Section 6.3. There are other occasional cases when extremely energetic solar flare generated shocks propagating through the interplanetary medium can accelerate the ambient particle population to higher energies. An example is the 4 August 1972 cosmic ray event thought to be the result of Fermi type acceleration of particles between two propagating interplanetary shock structures [Levy et al., 1976].

6.2.3 Geomagnetic Effects

Cosmic rays being charged nuclei experience a $\mathbf{V} \times \mathbf{B}$ force that continuously alters their path as they propagate through the geomagnetic field. When analyzing cosmic ray observations acquired on the earth to deduce the intensity and anisotropy of the cosmic ray flux in interplanetary space, it is necessary to make allowance for the "magnetic bending" of the cosmic ray trajectory through the magnetosphere. Methods that correct cosmic ray observations for the actual amount of the "geomagnetic bending" each particle has undergone are very specialized and beyond the scope of this handbook. Detailed information on cosmic ray asymptotic directions of approach, asymptotic cones, and variational coefficients is given by McCracken et al. [1965, 1968].

6.2.3.1 Cosmic Ray Cutoff Rigidities. Cosmic ray cutoff rigidities are values that specify the minimum rigidity a charged particle must possess to be observed at a specified position in the geomagnetic field from a specified direction. Rigidity is a canonical coordinate used in cosmic ray studies which is element independent. When translating these to the different elements of the cosmic ray spectrum, a different curve is obtained for each of the elements contained in the cosmic ray flux. If a primary cosmic ray particle is sufficiently rigid (that is, having a rigidity higher than the cutoff rigidity), it can penetrate through the geomagnetic field to an observation point; if the rigidity of the particle is less than the cutoff rigidity, it cannot penetrate through the magnetic field to the specified location from a specified direction. When considering charged particle propagation through the geomagnetic field, it is convenient to use the rigidity (momentum per unit charge) of the particle. To determine the energy per nucleon of a specific cosmic ray element, rigidity to energy tables can be utilized. See Section 6.1 for additional discussion.

Cosmic ray cutoffs are a function of geomagnetic latitude, altitude, and the zenith and azimuthal directions of the incident particle at the detection point. They have a maximum value in the earth's equatorial region and a minimum value in the polar regions. Unfortunately, the cosmic ray cutoff is not a simple value. There is an upper cutoff above which all particles are allowed, a lower cutoff below which all particles are forbidden, and a penumbral region between these two values where the transmission of cosmic

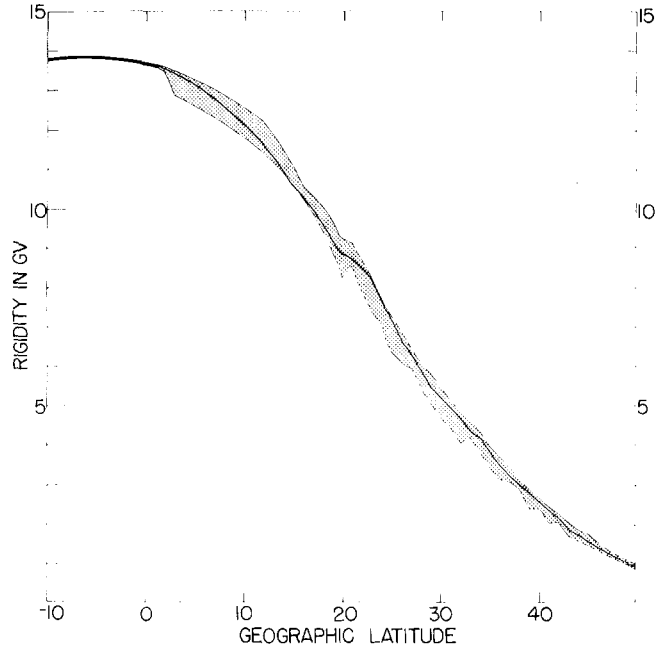

Figure 6-12. Illustration of the width (shaded area) of the cosmic ray vertical cutoff penumbra as a function of latitude along the 260°E meridian. The solid line indicates the effective geomagnetic cutoff rigidity along this meridian. The "sharpness" of the penumbral width variations are exagerated by only considering the vertical direction; however, the magnitude of the variation is correct.

radiation is chaotic. The cosmic ray penumbra exists near the cosmic ray cutoff rigidity where there is a complex series of allowed and forbidden particle trajectories that has so far defied all attempts to systematically order it. The effective cosmic ray cutoff is a practical value corrected for the transmission through the cosmic ray penumbra. An example of the variation of the vertical cosmic ray cutoff along the 260°E longitude meridian is shown in Figure 6-12. The width of the cosmic ray penumbra shown in this figure is somewhat typical of its worldwide behavior.

The primary reason that precise values of the cosmic ray cutoffs are relatively difficult to obtain is that the equation of charged particle motion in a magnetic field does not have a solution in closed form. Relatively accurate geomagnetic cutoff rigidities can be derived by the numerical integration of cosmic ray trajectories in mathematical models of the geomagnetic field; however, the calculation of these values for a large number of locations and directions involves a formidable amount of computational time. The precision of these calculations is limited only by the accuracy of the geomagnetic field model utilized.

There are long term secular variations in the cosmic ray cutoff rigidities directly reflecting the long term secular changes in the geomagnetic field. Over an approximate 10-yr period these changes are sufficient to be experimentally observed, and for very precise analyses these secular variations should be considered.

Because of the complexity of cutoff rigidity calculations, a number of approximations are generally employed. For experimental analyses, the specific approximation utilized is usually determined by the precision of the measurement being studied; as cosmic ray experiments become more precise, more accurate cutoff rigidities are required.

For the majority of cosmic ray studies on the earth's surface or in the atmosphere, it is often sufficient to know the vertical cutoff rigidity at each observational location. World grids of vertical cutoff rigidities from which values for intermediate locations and time periods can be inter-

Table 6-3. Trajectory-derived effective vertical cutoff rigidities for Epoch 1980.

Geographic Latitude	Geographic Longitude (E)											
	0	15	30	45	60	75	90	105	120	135	150	165
70	0.27	0.34	0.39	0.44	0.48	0.51	0.51	0.55	0.58	0.60	0.61	0.57
65	0.60	0.69	0.80	0.87	0.91	0.94	0.98	1.03	1.12	1.23	1.18	1.11
60	1.16	1.36	1.43	1.59	1.62	1.68	1.70	1.80	1.96	2.05	2.12	2.06
55	2.00	2.29	2.45	2.53	2.67	2.73	2.84	2.93	3.12	3.31	3.31	3.15
50	3.32	3.59	3.83	3.94	4.06	4.20	4.34	4.45	4.69	5.00	4.97	4.69
45	4.99	5.20	5.35	5.44	5.66	5.81	6.08	6.31	6.59	6.96	6.96	6.38
40	6.95	7.44	7.59	7.73	8.07	8.54	8.99	9.23	9.57	9.99	9.82	9.05
35	9.77	9.74	10.01	10.42	10.88	11.27	11.39	11.63	11.95	12.18	11.69	10.67
30	11.49	11.83	12.10	12.51	13.09	13.82	14.19	14.31	14.23	13.97	13.46	12.75
25	13.25	13.68	14.03	14.38	14.86	15.37	15.69	15.70	15.47	15.05	14.46	13.76
20	14.17	14.61	14.99	15.39	15.91	16.43	16.73	16.68	16.36	15.85	15.21	14.54
15	14.63	15.10	15.54	15.99	16.54	17.07	17.35	17.27	16.91	16.37	15.75	15.14
10	14.70	15.19	15.67	16.17	16.75	17.29	17.57	17.50	17.15	16.63	16.06	15.56
5	14.41	14.88	15.38	15.94	16.57	17.11	17.41	17.38	17.07	16.61	16.15	15.77
0	13.80	14.22	14.73	15.34	16.00	16.56	16.87	16.90	16.67	16.31	15.97	15.74
−5	12.94	13.27	13.77	14.41	15.10	15.64	15.97	16.07	15.94	15.68	15.50	15.42
−10	11.86	12.11	12.57	13.23	13.90	14.40	14.71	14.88	14.84	14.69	14.65	14.77
−15	10.45	10.63	11.08	11.75	12.32	12.80	13.06	13.24	13.17	13.18	13.39	13.69
−20	8.87	8.89	9.26	9.74	10.24	10.45	10.55	10.69	10.75	10.66	10.62	11.87
−25	7.28	7.29	7.63	7.93	8.02	7.71	7.28	7.26	7.42	7.64	8.36	9.49
−30	6.11	5.84	5.84	5.80	5.58	5.40	5.19	5.14	5.09	5.38	5.84	6.60
−35	5.05	4.49	4.37	4.38	4.12	3.85	3.47	3.41	3.34	3.55	4.10	4.90
−40	4.03	3.62	3.38	3.26	2.89	2.58	2.21	2.04	2.04	2.22	2.53	3.29
−45	3.33	2.88	2.53	2.38	2.00	1.54	1.28	1.12	1.10	1.22	1.47	2.01
−50	2.76	2.27	1.97	1.64	1.30	0.94	0.71	0.56	0.53	0.60	0.81	1.15
−55	2.17	1.72	1.45	1.12	0.82	0.56	0.35	0.24	0.21	0.25	0.38	0.57
−60	1.69	1.29	1.03	0.76	0.69	0.30	0.15	0.09	0.06	0.08	0.14	0.26
−65	1.29	0.96	0.72	0.48	0.29	0.14	0.06	0.00	0.00	0.00	0.03	0.10
−70	0.84	0.66	0.46	0.30	0.16	0.08	0.00	0.00	0.00	0.00	0.00	0.02

polated for Epochs 1955, 1965, 1975, and 1980 have been calculated by numerical integration [Shea et al., 1968; Shea and Smart, 1975; 1983]. An iso-rigidity contour map of effective vertical cosmic ray cutoffs for Epoch 1980.0, reflecting the use of the newer and more accurate internal magnetic field model [Peddie, 1982], is shown in Figure 6-13. The values for the effective vertical cosmic ray cutoff rigidities for this same epoch are tabulated in Table 6-3.

The Störmer Approximation. The classic work of Störmer on the motion of charged particles in a dipole magnetic field resulted in the following equation for the cosmic ray cutoff rigidity P_c

$$P_c = M\frac{\cos^4\lambda}{R^2[1 + (1 - \sin\varepsilon \sin\phi \cos^3\lambda)^{1/2}]^2} \quad (6.16)$$

where λ is the geomagnetic latitude, ε is the zenith angle, and ϕ is the azimuthal angle measured from the magnetic north. When this equation is normalized to the earth's dipole

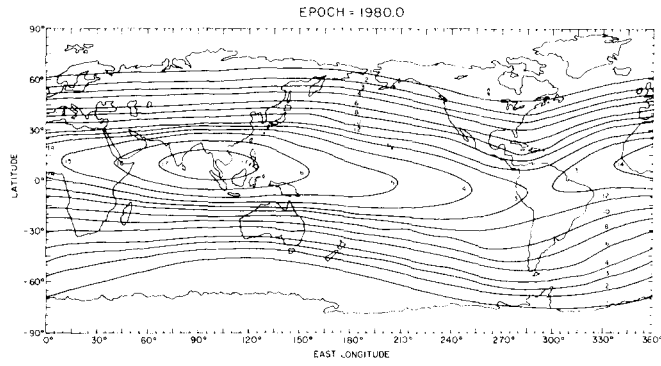

Figure 6-13. Iso-rigidity contours of vertical cosmic ray effective cutoff rigidities. The units of cutoff rigidity are in GV.

Table 6-3. (*Continued*)

Geographic Longitude (E)												
180	195	210	225	240	255	270	285	300	315	330	345	Geographic Latitude
0.47	0.36	0.23	0.13	0.04	0.00	0.00	0.00	0.00	0.06	0.11	0.19	70
0.99	0.77	0.49	0.31	0.17	0.09	0.05	0.05	0.09	0.17	0.30	0.43	65
1.76	1.38	0.98	0.65	0.40	0.23	0.16	0.16	0.23	0.39	0.64	0.90	60
2.85	2.28	1.75	1.23	0.81	0.49	0.36	0.36	0.50	0.80	1.21	1.70	55
4.25	3.46	2.81	2.05	1.42	0.98	0.75	0.73	0.95	1.43	2.13	2.85	50
5.60	4.85	4.15	3.16	2.37	1.75	1.35	1.27	1.62	2.47	3.35	4.35	45
7.96	6.47	5.49	4.60	3.63	2.77	2.14	2.05	2.57	3.79	5.08	6.15	40
9.52	8.99	7.67	6.11	5.17	4.21	3.24	2.99	3.83	5.26	7.36	9.11	35
11.69	10.48	9.65	8.78	6.99	5.54	4.38	4.02	5.14	7.54	10.02	10.94	30
13.04	12.38	11.74	10.88	9.63	7.74	6.02	5.51	7.02	9.98	11.78	12.68	25
13.90	13.33	12.84	12.23	11.32	9.35	7.67	6.61	8.49	11.67	12.88	13.63	20
14.59	14.09	13.67	13.19	12.46	11.05	9.27	8.64	11.01	12.60	13.50	14.12	15
15.10	14.68	14.30	13.88	13.35	12.36	11.27	11.06	12.22	13.11	13.78	14.25	10
15.43	15.07	14.73	14.36	13.92	13.22	12.45	12.29	12.73	13.33	13.76	14.04	5
15.53	15.25	14.93	14.60	14.21	13.71	13.14	12.80	12.97	13.32	13.48	13.55	0
15.35	15.17	14.92	14.62	14.28	13.86	13.36	12.99	12.98	13.09	13.00	12.85	−5
14.87	14.82	14.66	14.43	14.15	13.81	13.37	12.97	12.81	12.69	12.36	11.92	−10
14.01	14.17	14.15	14.03	13.84	13.57	13.19	12.77	12.47	12.15	11.53	10.79	−15
12.72	13.15	13.36	13.42	13.35	13.17	12.85	12.42	11.99	11.47	10.49	9.47	−20
10.19	11.24	11.98	12.56	12.67	12.63	12.38	11.94	11.40	10.52	9.35	8.04	−25
7.98	9.45	9.40	10.75	11.79	11.92	11.78	11.34	10.56	9.57	8.15	6.88	−30
5.65	6.62	8.01	8.73	9.62	11.05	11.09	10.55	9.73	8.50	6.88	5.95	−35
4.15	4.84	5.60	6.76	8.18	9.73	10.08	9.63	8.80	7.35	6.18	5.00	−40
2.69	3.30	4.28	4.99	6.01	7.87	8.89	8.52	7.74	6.80	5.34	4.15	−45
1.65	2.24	2.94	3.79	4.58	5.61	7.05	7.41	6.77	5.47	4.27	3.42	−50
0.95	1.36	1.94	2.64	3.35	4.29	4.90	5.18	4.90	4.25	3.48	2.77	−55
0.51	0.76	1.20	1.77	2.27	2.98	3.75	4.01	3.82	3.39	2.72	2.14	−60
0.22	0.42	0.69	1.05	1.55	1.96	2.46	2.72	2.63	2.40	2.02	1.61	−65
0.10	0.22	0.40	0.60	0.90	1.20	1.51	1.67	1.75	1.59	1.33	1.11	−70

moment M and the distance from the dipole center R is expressed in earth radii, the constant terms evaluate to 59.6. For locations on the earth the vertical cutoff rigidity is very useful, and since the zenith angle is zero the dipole vertical cutoff is given by

$$P_c = \frac{14.9 \cos^4\lambda}{R^2}. \qquad (6.17)$$

Variations of the Störmer cutoff equation can be employed when normalized to the earth's actual magnetic field. An improvement in accuracy can be obtained by correcting for the displacement of the earth's effective magnetic center from the geocenter. A number of magnetic coordinate systems can be employed; however, the McIlwain B-L coordinate system [McIlwain, 1961] is very useful since in a dipole field $\cos^2\lambda = R/L$. The worldwide grid of trajectory-derived effective vertical cosmic ray cutoff rigidities, normalized to the L parameter, results in

$$P_c = 16.0\, L^{-2}. \qquad (6.18)$$

This form is useful where the geomagnetic field retains its basic dipolar structure; it can be used throughout the magnetosphere wherever a useful L coordinate can be calculated. A practical limit for the region of applicability seems to be within the domain of the L = 4 shell. At higher L-shells increasing errors will be encountered due to the external current systems of the magnetosphere.

Recent work indicates that the Störmer equation can be generalized to estimate the cutoff at other directions and altitudes if a local normalization value is available. If a vertical (more properly, dipole radial) cutoff is known, the cutoff at other directions may be computed using a normalized form of Equation (6.16) and an appropriate magnetic coordinate system. If a cutoff at one altitude is known, the cutoff at another altitude can be computed. A convenient way is to employ the L^{-2} dependence of Equation (6.18).

Cosmic Ray Cutoffs at High Latitudes. The earth's magnetosphere has a dynamic topology reflected in the daily variation of the cosmic ray cutoff at high magnetic latitudes. In regions where the magnetic field lines are "open" (that is, traceable to the distant magnetospheric tail), the cosmic ray cutoff is essentially zero. In regions of the magnetosphere where the magnetic field line topology changes from open to closed as the earth rotates (magnetic latitudes from ~ 60° to ~ 75°), there is a significant daily variation in the value of the cosmic ray cutoff rigidities. Current magnetospheric models are inadequate to precisely model these changes and are limited to providing upper limits of the cutoff rigidity values. The best available average high latitude cutoff values have been obtained by polar orbiting satellites [Fanselow and Stone, 1972] and are shown in Figure 6-14.

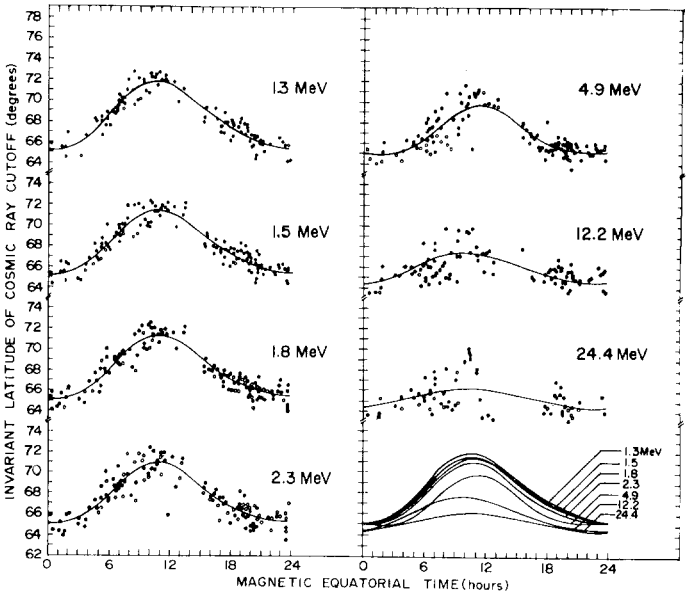

Figure 6-14. Daily variation of the high latitude geomagnetic cutoffs.

6.2.4 Charged-Particle Flux Within the Atmosphere

The intensity and composition of the cosmic rays observed within the atmosphere depend on the quantity of absorbing material traversed before observation in addition to the cutoff rigidity of the observation point. Atmospheric conditions, especially barometric pressure, have an appreciable effect on the measured intensity; hence, cosmic-ray intensities are usually reported in terms of atmospheric depth (mass of air per unit area above the observation point) or of air pressure at the observation point rather than the altitude of the observation. The ionization rate measured within the atmosphere depends upon the amount of matter above the point of observation and on its distribution in height. At a given altitude, the value of the pressure in millibars is about 2% less than the atmospheric depth in grams per square centimeter. Figure 6-15 is a plot of atmospheric depth as a function of altitude.

Primary cosmic rays incident upon the top of the earth's atmosphere interact with air nuclei producing high-energy secondary cosmic rays. These secondary particles, in turn, interact with other nuclei and produce additional secondaries. Figure 6-16 illustrates a nuclear cascade process initiated by a primary cosmic ray. The production of secondary components becomes significant at about 55 km (4-mb pressure with the local intensity reaching a maximum (the Pfotzer maximum) at approximately 20 km (56 mb). The intensity of secondaries then decreases from the Pfotzer maximum to the surface of the earth as the particles lose energy by additional collisions until the majority either decay or are absorbed. An excellent compilation assembling cosmic ray

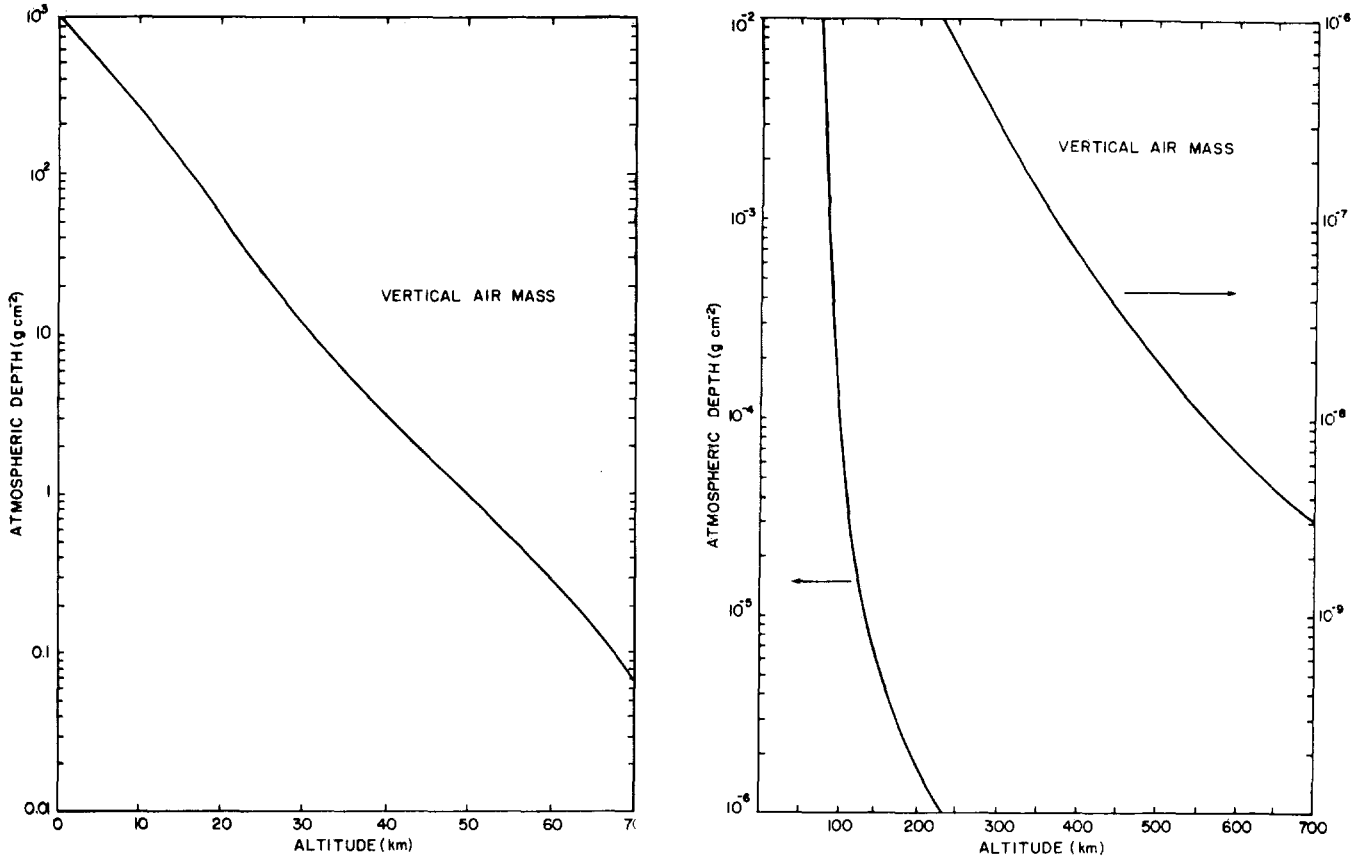

Figure 6-15. The mass of air per unit area in a vertical column extending upward from a height H above sea level [Ely, 1962].

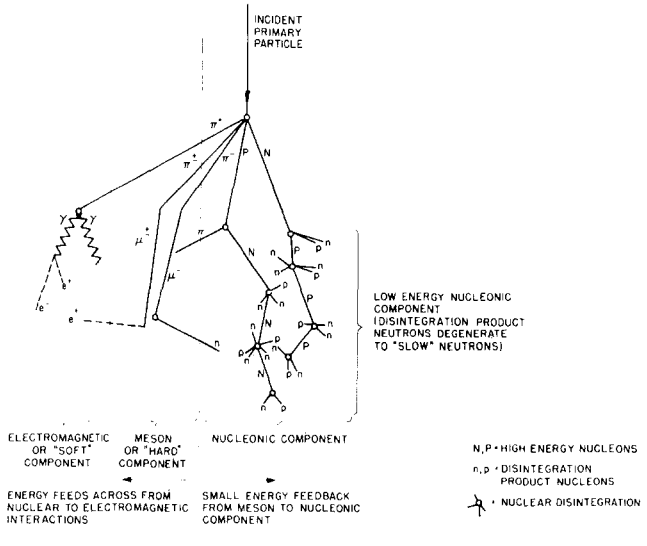

Figure 6-16. Schematic diagram of a cosmic ray shower. N and P are high energy neutrons and protons while the lower case n and p are used to denote disintegration product neutrons and protons. Pions, mesons, electrons, positrons, and gamma rays are indicated by conventional symbols.

observations on the earth has been prepared by Allkofer and Grieder [1984].

In theory, the intensity of any specified secondary component can be derived from a knowledge of the primary spectrum and the specific yield functions. Computer codes exist that will convert a specified primary cosmic ray spectrum into probable secondary components at any location and specified atmospheric depth. See O'Brien [1970], O'Brien [1979] and references therein. An example of the computed and experimentally measured ionization as a function of altitude is shown in Figure 6-17.

6.2.4.1 The Secondary Cosmic Ray Ionizing Component. The cosmic ray secondaries most commonly measured on the earth's surface are π and μ mesons, neutrons, protons, electrons, and γ-ray photons. The secondary cosmic rays are often classified into three major components: the hard component comprised of primarily relativistic muons, the nucleonic component comprised of locally produced protons and neutrons and the soft component, comprised of electrons and γ rays. The flux and composition of the secondary cosmic rays are the result of random interaction probabilities; the instantaneous flux of ionizing secondaries can have a considerble variation from the average flux. For

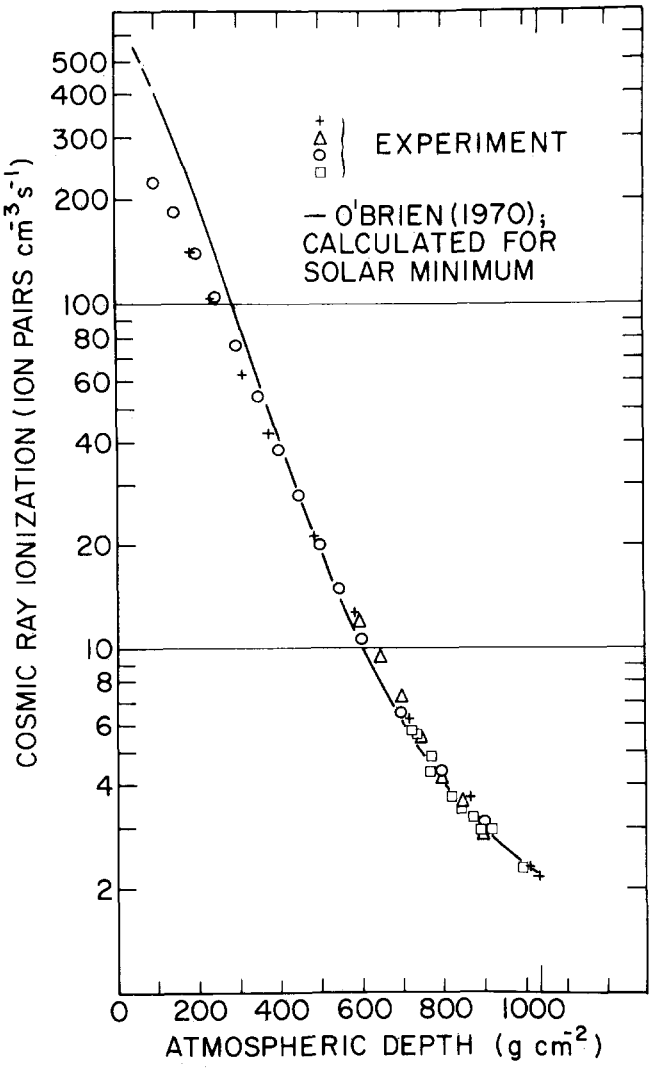

Figure 6-17. Computed and experimental altitude variation of cosmic ray ionization. The data are normalized to a sea level value of 2.15 ion pairs per second per cubic centimeter at sea level [Kykler and Liboff, 1978].

example the intensity in the core of the cosmic ray shower may be orders of magnitude above the "average" for a few microseconds.

Typical ionization rates in the polar atmosphere as a function of atmospheric depth and solar-cycle variation are shown in Figure 6-18. The variation of ionization with latitude obtained by Neher [1967] during the 1965 solar minimum, plotted as a function of cosmic ray cutoff rigidity, is illustrated in Figure 6-19. The most common high energy ionizing component of the secondary cosmic radiation is the cosmic ray μ meson. These muons must be relativistic to traverse the atmosphere (half life $= 2 \times 10^{-6}$ s), are only weakly ionizing (the energy loss of a μ meson in air is 2.2 MeV cm^2 g^{-1}) and at sea level have a pole to equator latitude dependence of the order of $\sim$ 10%. The typical μ meson spectrum is shown in Figure 6-20. The μ meson intensity as a function of altitude is shown in Figure 6-21.

The high energy secondary cosmic radiation can initiate nuclear interactions in whatever matter they penetrate. The nuclear fragments of these interactions resemble "stars" when recorded in photographic emulsions and examined under high magnification. "Star counts" can be used to estimate the probable rate of interactions in semi-conductors; these interactions can cause errors in solid state logic circuits. A compact tabulation of observed star counts is given in Table 6-4.

6.2.4.2 The Secondary Cosmic Ray Neutron Component. The secondary cosmic ray neutron component is generated within the atmosphere by the nuclear interaction of high energy cosmic ray nuclei with atmospheric atoms. There are no neutrons in the primary cosmic ray flux. At high energies the "knock-on" process dominates the neutron production, while at lower energies the "neutron evaporation" process dominates the neutron production. These neutrons interact with other atmospheric atoms and produce radioactive isotopes. The secondary neutron flux in the atmosphere is responsible for the generation of cosmogenic isotopes such as ^{14}C (half life of 5730 years), ^{26}Al (half life

Table 6-4. Cosmic ray induced nuclear interactions (per cubic centimeter per day).

Type of Star (Number of Prongs)	2 GV Cutoff Rigidity						10 GV Cutoff Rigidity	
	Atmospheric Depth (g/cm^2)						Atmospheric Depth (g/cm^2)	
	14.9	47.4	63.7	81.3	121	677	14.9	47.4
>2	2390	2030	2150	2040	1610	22.0	575	425
>9	618	352	372	235	290	1.2	238	132
>16	223	122	128	27	116	0.29	105	61

[Data sources: Rossi [1952; 1964] and references therein.]

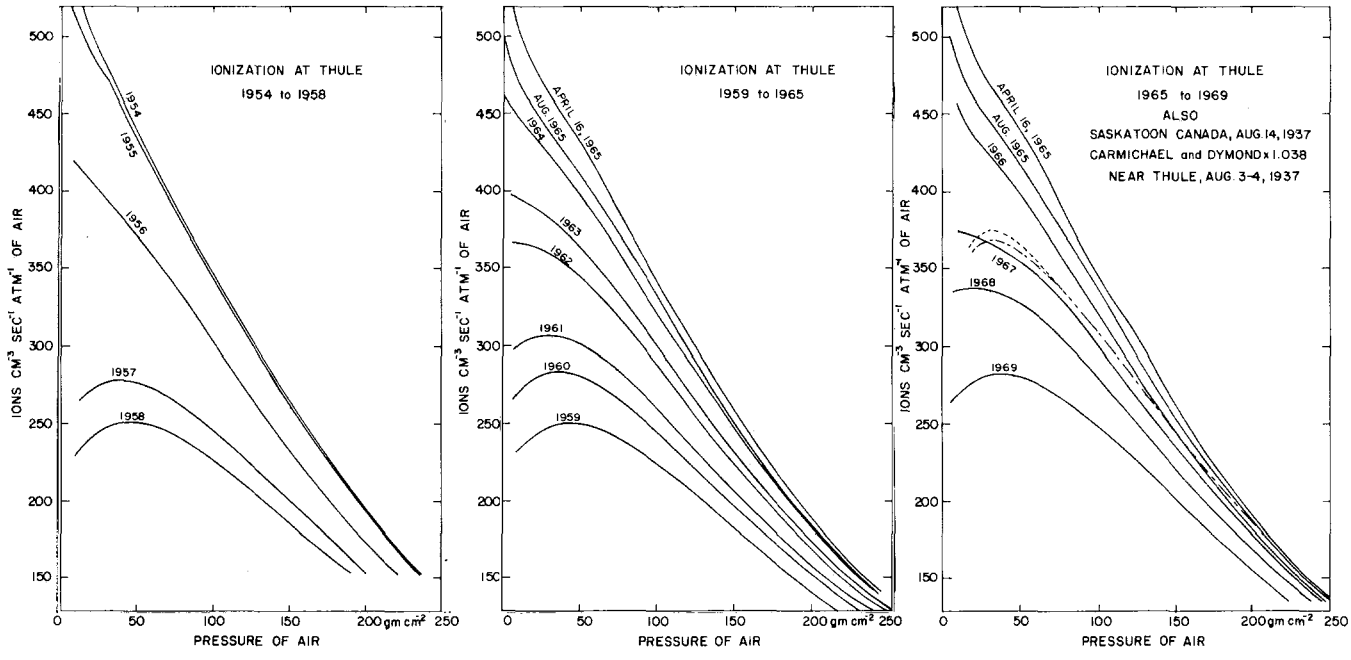

Figure 6-18. Yearly averaged cosmic ray ionization rate per atmosphere of air as a function of atmospheric depth [Neher, 1971].

of 7.4 × 10^5 years), and ^{10}Be (half life of 1.5 × 10^6 years). The carbon-14 isotope enters the biosystem and can be used to date dead biological materials. Other long lived isotopes may collect in the polar ice or sea sediments. The differential energy spectrum of neutrons at various depths in the atmosphere is shown in Figure 6-22 [Armstrong et al., 1973]. These results are typical of midlatitudes. The fast neutron flux in the atmosphere at various depths and cutoff rigidities for both solar minimum and solar maximum conditions is illustrated in Figure 6-23 [Light et al., 1973].

6.2.5 Cosmic Ray Albedo

Some small fraction of the secondary cosmic radiation will escape the atmosphere and contribute to the total radiation flux exposure to earth orbiting satellites. The electrons and protons will spiral along the earth's magnetic field lines to the opposite hemisphere. Measurements of the albedo proton flux at the "top" of the atmosphere for high and midlatitudes are given in Figure 6-24 while the albedo electron flux at the "top" of the atmosphere is given in Figure

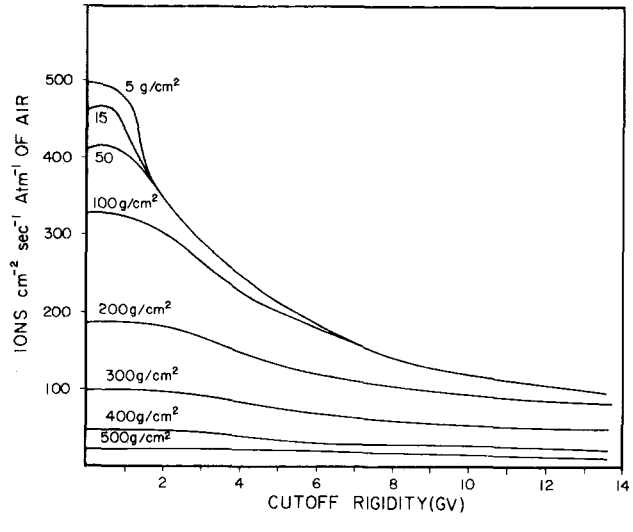

Figure 6-19. Cosmic ray ionization rate as a function of altitude and geomagnetic cutoff rigidity.

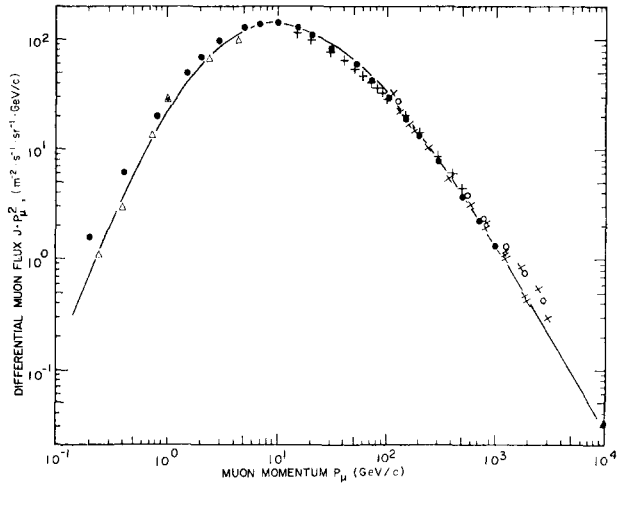

Figure 6-20. Differential vertical flux of muons at sea level. Measured values are indicated by the various symbols while the solid line is a mathematical calculation. [Murakami et al., 1979].

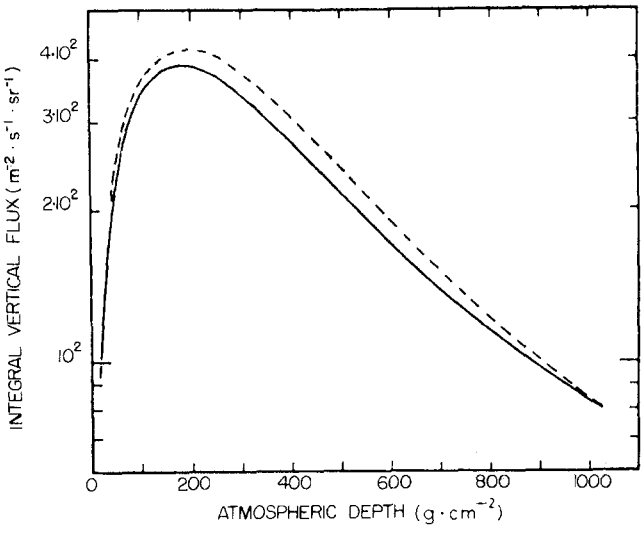

Figure 6-21. Altitude variation of the muon intensity >0.3 GeV. The solid line represents older values (circa 1948) [Murakami et al., 1979].

6-25. The electron albedo includes approximately equal numbers of electrons and positrons. There appears to be a large variability in the available electron albedo measurements that is not yet resolved. Typical numbers in the energy range 0.1 to 2.5 GeV are $e^+ = 77, e^- = 67\ m^{-2}s^{-1}sr^{-1}$. The results of satellite measurements in the equatorial region at 230 km are given in Figure 6-26. There is an approximate factor of 2 increase in these numbers in the high latitude region.

About 10% of the secondary cosmic ray neutron flux in the upper atmosphere will escape into space. The cosmic ray albedo neutron flux escaping from the atmosphere is not bound by the earth's magnetic field and will later decay (neutron half life ~ 11.7 minutes) into an electron and proton, which may be trapped in the earth's magnetic field, and an anti-neutrino. The albedo neutron flux is an important source of the high energy proton flux trapped in the earth's magnetosphere (see Chapter 5). A model "global averaged" albedo neutron spectrum is given in Figure 6-27. Near the earth there is an approximate 1:7 ratio of the albedo neutron flux from the equatorial atmosphere as compared with the flux from the polar atmosphere.

6.3 ENERGETIC SOLAR PARTICLES (SOLAR COSMIC RAYS)

Part of the energy released in solar flares may be nuclei accelerated to high energies and released into space. These solar particle events are commonly referred to by a number of descriptive names such as solar cosmic ray events (SCR), solar proton events, solar electron events, polar cap absorption events (PCA), and ground level events (GLE). Each of these names results from and is descriptive of a measurement technique. Cosmic ray sensors on the earth recorded the first observed energetic solar flare particle outbursts, and hence the name solar cosmic ray events was derived. Later, when balloon borne cosmic ray detectors observed particle events not detected at the earth's surface, the name ground level event was introduced to distinguish between those events detected at ground level and those observed only near the top of the atmosphere. This name is still used to identify solar particle events containing relativistic protons. Beginning in the 1950s the earth's polar ionosphere was shown to respond to solar flare protons with energies from about 1 to 50 MeV, and the term PCA events became synonymous with solar proton events. Spacecraft measurements are now many orders of magnitude more sensitive than earth-based measurements and allow measurements of the composition of solar particle events. The term solar electron event was introduced after 1965 to distinguish the species of particles present. However, the older definitions are still used to provide continuity of historical data bases.

The most commonly measured components of solar particle events are protons and electrons. The first positive measurements of solar neutrons occurred in 1980 [Chupp et al., 1982]. Solar neutron fluxes at the earth will be extremely rare as the neutron half life of ~ 11.7 min implies all but the most energetic solar neutrons will have decayed before they can reach the earth's orbit.

6.3.1 The Solar Particle Source

The source of the energetic solar particles is generally the solar flare (see Chapter 1). There is a time correlation between the observation of an increase of the particle flux in interplanetary space and the occurrence of a solar flare. At low energies, there is a correspondence between the level of solar activity (such as the number of flares and sub-flares) and the low energy solar particle flux in interplanetary space. Some flares are more copious energetic particle producers than others, the more copious solar particle generators generally being solar flares rich with x-ray and high frequency radio emission (particularly in the centimeter and millimeter wave lengths).

Many of the particles accelerated to high energies in a solar flare will escape from the solar corona into the interplanetary medium. As the energetic charged particles move into the interplanetary medium they will be guided along the existing spiral magnetic field pattern. As a result, both the intensity and the spectrum observed at the earth depend somewhat on the relative positions of the earth and the flare on the sun. For example, a solar wind velocity of 400 km/s produces a spiral field that connects the earth to the solar longitude ~ 55° west of the central meridian of the sun as viewed from the earth. The actual degree of "well connectedness" between the earth and the sun depends on in-

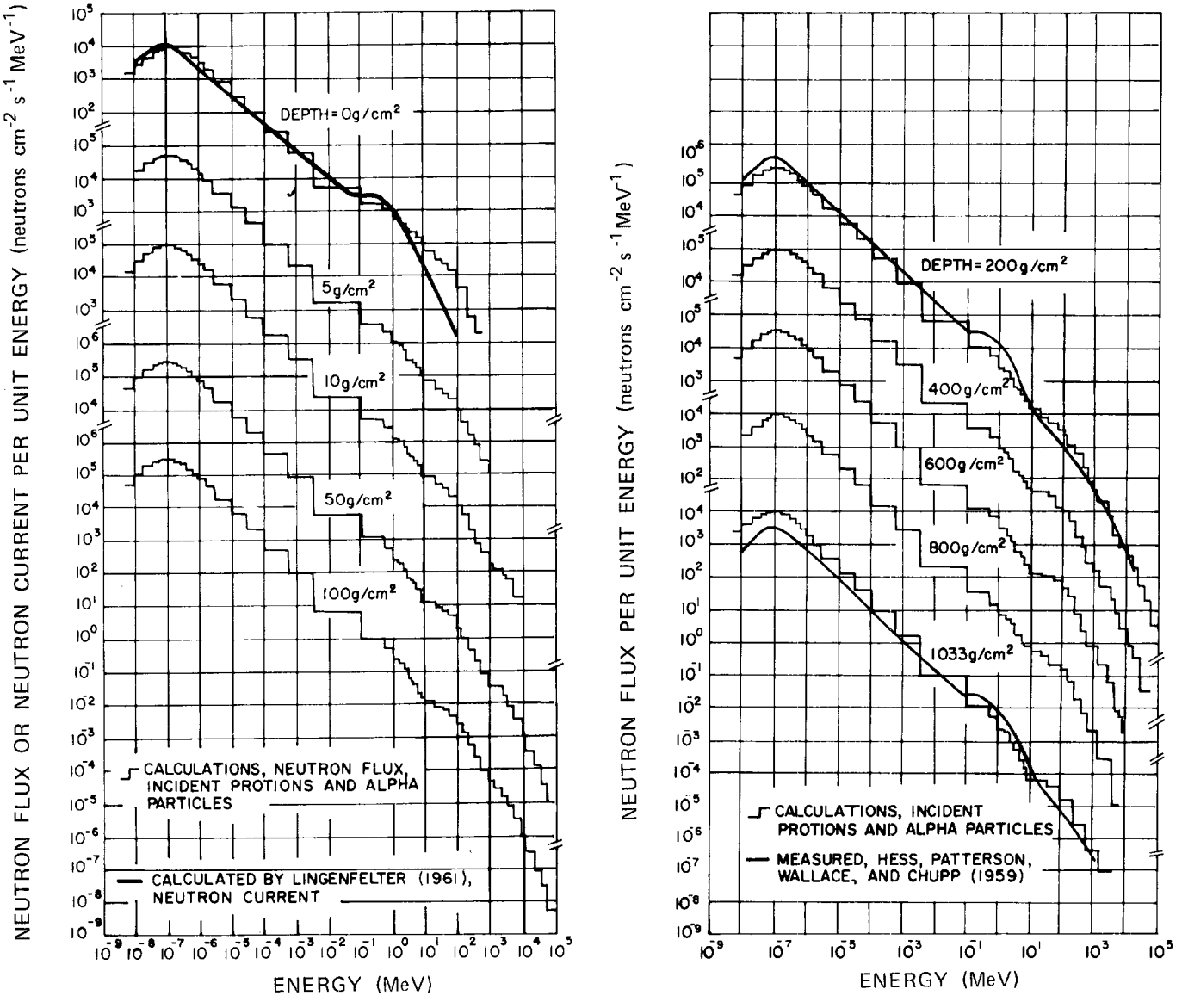

Figure 6-22. Neutron spectra at various depths from the top of the atmosphere. The data are adjusted to solar minimum conditions at the midlatitude geomagnetic latitude of ~42°, (equivalent to a vertical cutoff rigidity of 4.5 GV).

terplanetary conditions at the time of the flare, and these conditions are highly variable and unpredictable.

6.3.2 The Size and Frequency of Solar Particle Events at the Earth

Major solar particle events occur at random, with a frequency that varies from approximately one every two months to one every two years. Major solar particle events consist primarily of sizeable fluxes of energetic electrons and energetic protons. These solar flare initiated solar particle events may also contain a small and apparently variable flux of heavier elements. The frequency of solar particle events is correlated with the solar activity cycle; however, there is a large variance in the distribution. Significant solar particle events have occurred during solar minimum. There can be relatively long periods between significant solar particle events during the solar maximum. The elemental composition of the accelerated ions is not radically different from the elemental composition of the solar atmosphere, although composition differences as a function of energy exist as discussed in Section 6.3.3. The "size" of a solar particle event depends on the energy of measurement, and consequently the "size" is dependent on the energy spectra. The particle events near the earth that result from these solar flares may last from a few hours up to a maximum of approximately ten days. The *Catalog of Solar Proton Events*

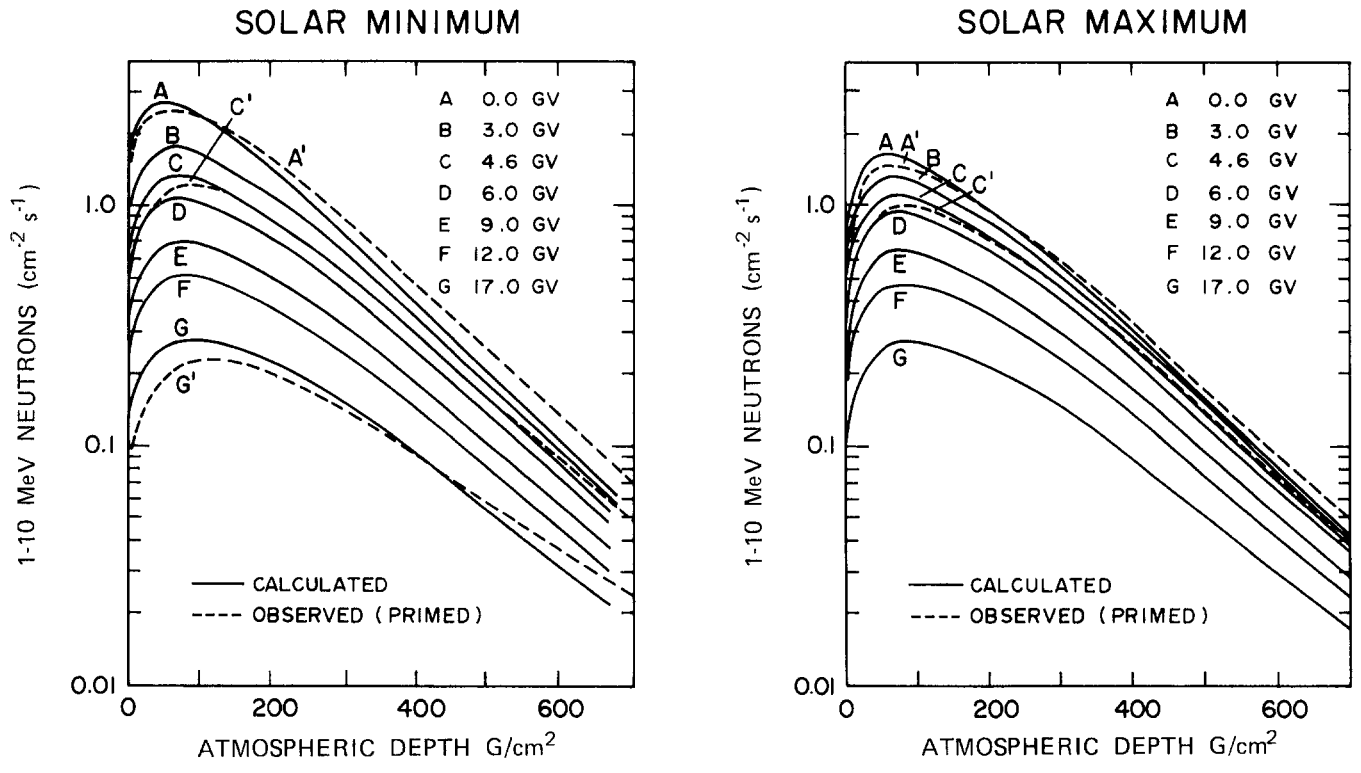

Figure 6-23. Fast neutron flux versus atmospheric depth for various cutoff rigidities for solar minimum conditions (left panel) and solar maximum conditions (right panel).

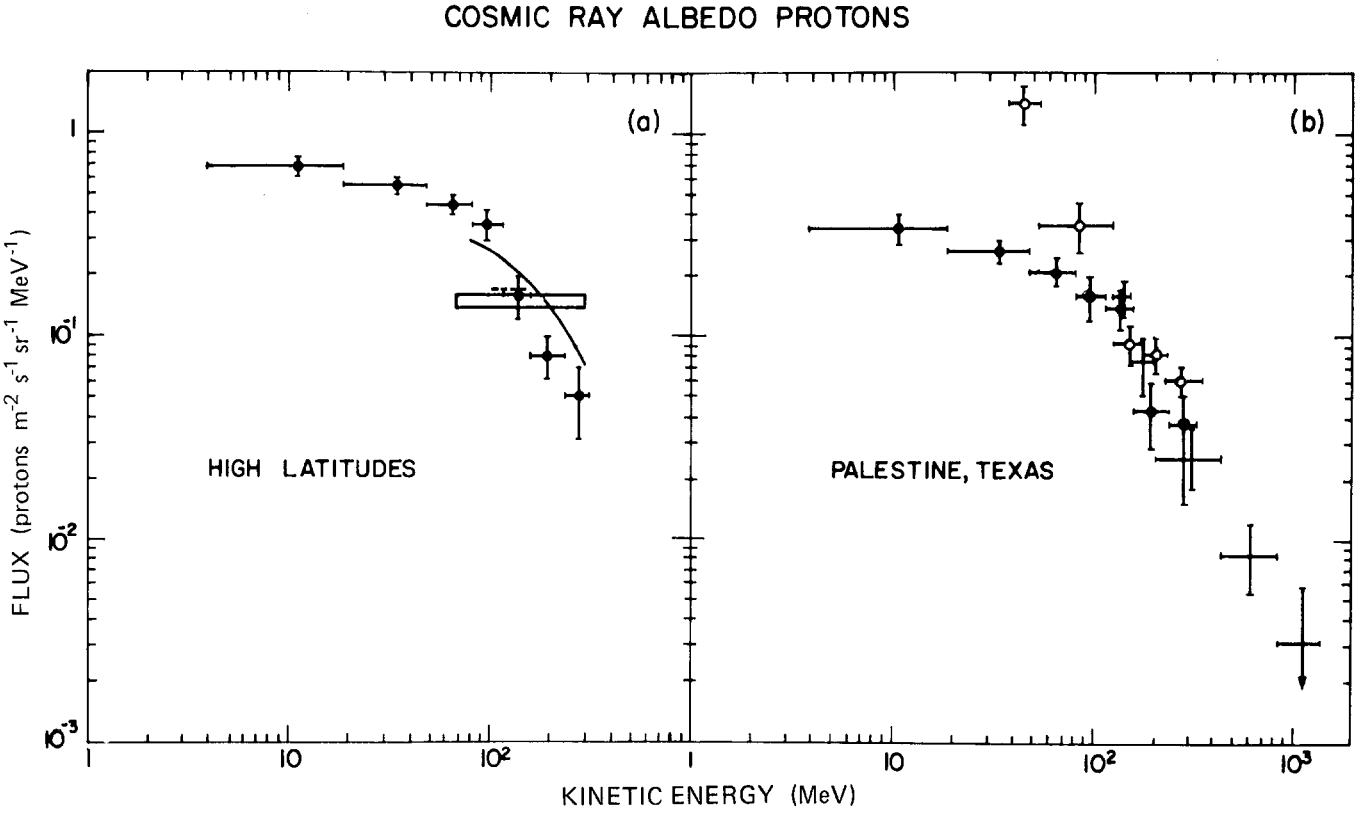

Figure 6-24. Measured differential energy spectrum of the albedo proton flux at the "top" of the atmosphere, at two different locations [Wenzel et al., 1975].

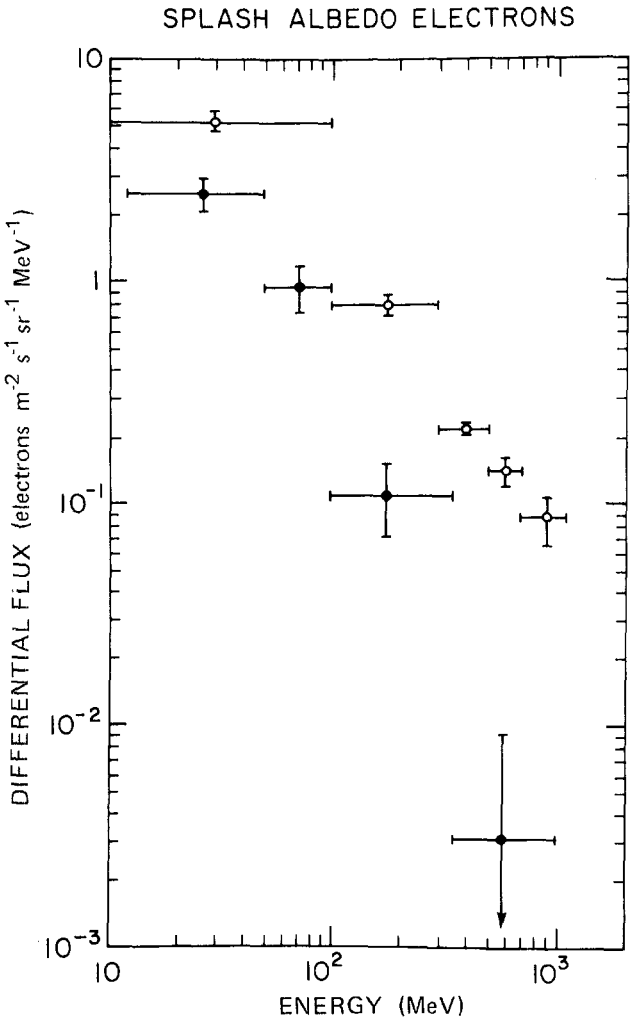

Figure 6-25. Measured differential kinetic energy spectrum of the albedo electron flux at the "top" of the atmosphere. The solid circles are measurements at Palestine, Texas (vertical cutoff rigidity ~4.5 GV), and the open circles are measurements at high latitudes (Ft. Churchill, Canada). Adapted from Israel [1969].

1955–1969 [Dodson et al., 1975] and *Catalog of Solar Proton Events 1970–1979* [Akiniyan et al., 1983] contain considerable detail in describing solar particle events and associated solar circumstances.

6.3.2.1 Solar Proton Events. A list of the major solar proton events observed at 1 AU at the orbit of the earth is given in Table 6-5. The solar proton event frequency distribution has a period of ~ 11 years (the solar sunspot cycle), and there is usually one anomalously large event in each solar cycle. Apart from these anomalous events, the remaining events seem to be distributed as though the log (to base 10) of their sizes has a normal statistical distribution. This is called a log-normal distribution. King [1974] has found that the distribution of the solar proton fluences F is a log-normal distribution above any energy threshold. The

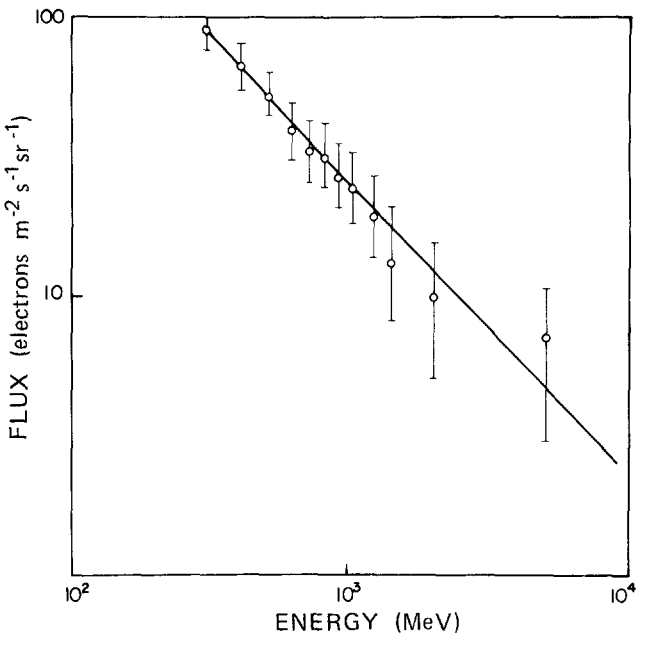

Figure 6-26. Spacecraft measurements of the low altitude albedo electron flux [Kurnosova, 1978].

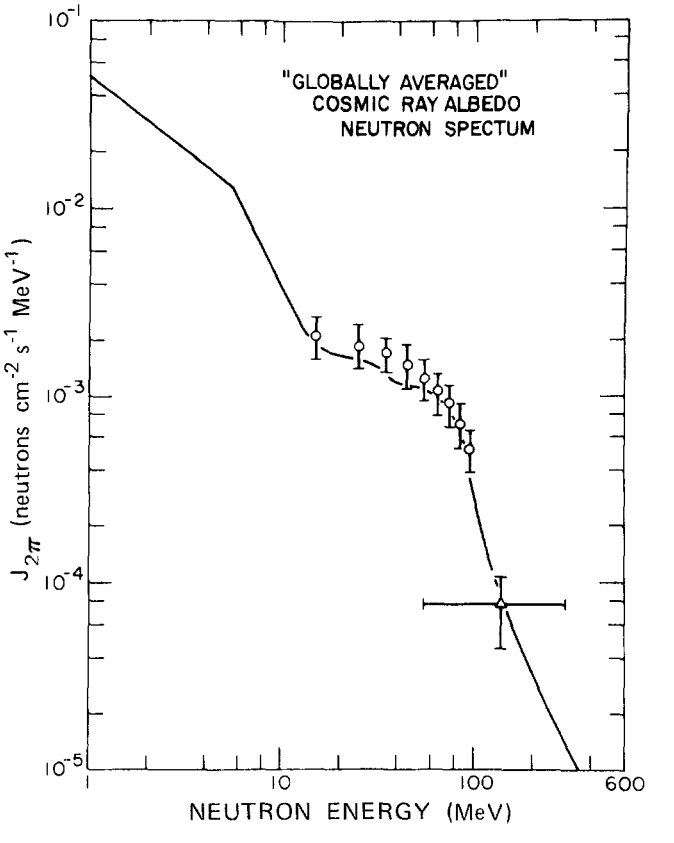

Figure 6-27. A model "global averaged" albedo neutron spectrum [Claflin and White, 1974].

Table 6-5. Major solar proton events observed at the earth.

Solar Particle Event Onset Date	PECS	Maximum Neutron Monitor Increase (Percent)	Maximum 30 MHz Riometer Absorption (db)	Peak Flux (cm^{-2} s^{-1}) (onmidirectional) >30 MeV	Integrated Intensity (cm^{-2}) >30 MeV
1956 Feb 23	X 3 4	4554	13	6 200*	6.5×10^{8}*
1956 Aug 31	X 3 0	—	4.9	150*	2.5×10^{7}*
1957 Jan 20	X 2 0	—	4.1	2 500*	3×10^{8}*
1958 Mar 23	X 2 0	—	3.2	1 200*	[2×10^{8}]†*
1958 Mar 25	X 3 0	—	10	1 500*(sc)	
1958 Jul 7	X 4 0	—	23.7	1 500*	3×10^{8}*
				2 000*(sc)	
1958 Aug 16	X 4 0	—	>15	200*	2×10^{7}*
1958 Aug 22	X 3 0	—	10.6	500*	5×10^{7}*
1958 Aug 26	X 4 0	—	16.6	1 100*	5.3×10^{7}*
1958 Sep 22	X 3 0	—	10.6	50*	6×10^{6}*
1959 May 10	X 4 0	—	22	6 000*	7×10^{8}*
				8 000*(sc)	
1959 Jul 10	X 4 0	—	20	4 000*	8.8×10^{8}*
1959 Jul 14	X 4 0	—	23.7	11 000*	1.1×10^{9}*
1959 Jul 16	X 4 2	10	21.2	16 000*	8.1×10^{8}*
				18 000(sc)	
1960 Apr 1	1 2 0	—	3	50*	2.7×10^{6}*
1960 Apr 5	1 2 0	—	3.1	40*	2×10^{6}*
1960 Apr 28	(2)2 0	—	3	300*	2.5×10^{7}*
1960 May 4	(1)2 4	290	5	200*	7×10^{6}*
1960 May 13	(1)2 0	—	4.5	60*	4×10^{6}*
1960 Sep 3	2 2 1	4	2.7	240*	4×10^{7}*

Date	PECS	Maximum Neutron Monitor Increase (Percent)	Maximum 30 MHz Riometer Absorption (db)	Peak Flux (cm^{-2} s^{-1}) directional >30 MeV	Peak Flux (cm^{-2} s^{-1}) onmidirectional >30 MeV	Integrated Intensity (cm^{-2}) >30 MeV
1960 Nov 12	4 4 4	135	21.2		12 000*	1.4×10^{9}*
1960 Nov 15	4 4 3	88	>20		6 000*	5.2×10^{8}*
1960 Nov 20	(3)3 2	8	5		1 000*	6×10^{7}*
1961 Jul 11	X 1 0	—	1		20*	2×10^{6}*
1961 Jul 12	(2)4 2	—	17		120*	1.0×10^{8}*
1961 Jul 18	3 3 3	24	11		2 500*	2.1×10^{8}*
1961 Jul 20	(1)2 2	7	5		300*	9×10^{6}*
1961 Sep 28	2 2 0	—	3.3	11.0	150*	2.4×10^{6}*
1963 Sep 20	1 2 0	—	4	4.0	30	1×10^{6}
1965 Feb 5	1 1 0	—	1.3	50.0	250	1×10^{6}
1966 Mar 24	1 2 0	—	1.6	15.0		$\sim 1.0 \times 10^{5}$
1966 Jul 7	1 2 1	3	2.1	30.0		4.4×10^{5}
1966 Aug 28	1 2 0	—	4	15.0		1.0×10^{5}
1967 May 25	3 3 0	—	11	32.0		1.7×10^{6}
1967 May 28	2 2 0	—	4.1	27.0		1.3×10^{6}
1967 Dec 3	1 2 0	—	1.8	10.5		4.6×10^{5}
1968 Jun 9	2 3 0	—	6.5	12.4		8.9×10^{5}
1968 Sep 28	1 1 0	—	1.2	0.1		[6.9×10^{5}]†
1968 Sep 29	1 2 1	1	1.7	19.0		

Date	PECS	Maximum Neutron Monitor Increase (Percent)	Maximum 30 MHz Riometer Absorption (db)	Peak Flux (cm^{-2} s^{-1} sr^{-1}) (directional) >30 MeV	Integrated Intensity (cm^{-2}) >30 MeV
1968 Oct 4–6	1 2 0	—	1.5	6.3	2.6×10^5
1968 Oct 31	2 3 0	—	5.5	10.0	
					[1.2×10^6]†
1968 Nov 1	2 3 0	—	4	11.7	
1968 Nov 18	2 3 3	14	12.5	404.0	1.7×10^7
1968 Dec 3	1 2 0	—	(slight)	1.7	
					[3.2×10^6]†
1968 Dec 5	2 3 0	—	4.7	31.0	
1969 Feb 25	1 2 3	16	2.1	41.5	2.1×10^6
1969 Mar 30	1 1 2	9	1.4	13.0	1.3×10^6
1969 Apr 11	3 3 0	—	>16	123.0	1.6×10^7
1969 Nov 2	3 3 0	—	13	737.0	2.1×10^7
1970 Jan 31	1 2 0	—	3	6.2	2.7×10^5
1970 Mar 6	1 3 0	—	5	0.9	1.0×10^5
1970 Mar 29	1 2 0	—	1.8	20.2	1.7×10^6
1970 July 24	1 2 0	—	4.5	0.8	5.8×10^4
1970 Aug 14	2 2 0	—	3.0	2.7	3.9×10^5
1970 Nov 5	1 2 0	—	3.5	1.7	2.8×10^5
1971 Jan 24	3 3 3	26	14.5	408.0	2.7×10^7
1971 Apr 6	1 2 0	—	3.8	5.0	2.0×10^5
1971 Sep 1	2 3 3	16	5.2	162.0	1.3×10^7
1972 May 28	1 2 0	—	2.6	2.7	5.3×10^5
1972 Aug 4	4 4 2	20	>22	21 000.0	6.2×10^8
1972 Aug 7	3 4 2	8	3.1	384.0	3.0×10^7

PECS. The notation PECS stands for the three digit proton event classification system as defined by Smart and Shea [1971] as follows:

First Digit	Second Digit	Third Digit
E > 10 MeV Satellite Measured Proton Intensity Digit $cm^{-2}s^{-1}sr^{-1}$	Daylight Polar 30 MHz Riometer Absorption	Sea Level Neutron Monitor Increase
−3 From 10^{-3} to 10^{-2}	—	—
−2 From 10^{-2} to 10^{-1}	—	—
−1 From 10^{-1} to 10^{0}	—	—
0 From 10^{0} to 10^{1}	No measurable increase	No measurable increase
1 From 10^{1} to 10^{2}	Less than 1.5 dB	Less than 3%
2 From 10^{2} to 10^{3}	From 1.5 dB to 4.6 dB	From 3% to 10%
3 From 10^{3} to 10^{4}	From 4.6 dB to 15 dB	From 10% to 100%
4 Greater than 10^{4}	Greater than 15 dB	Greater than 100%

The first digit represents the measurement of the E > 10 MeV proton flux by a satellite within the earth-moon system, the second digit represents the 30 MHz absorption measured by a sunlit polar riometer, and the third digit represents the response of a high latitude sea level neutron monitor. An "X" in the first digit indicates that not enough satellite data are available to make a determination of the maximum flux of protons greater than 10 MeV. A digit within parenthesis is provisional, based on partial data.

*Proton flux data derived from Polar Cap absorption measurements.

(sc) Peak flux associated with geomagnetic storm.

[ ]† Composite integrated proton flux of 2 separate events.

Table 6-6. The parameters of the log-normal distributions for ordinary solar flares. Parameters are shown for the integral omnidirectional fluence for the entire solar event in protons cm^{-2}, and the peak omnidirectional flux in protons cm^{-2} s^{-1}.

	E > 10 MeV	E > 30 MeV	E > 60 MeV	E > 100 MeV
Log Omnidirectional Integral Fluence (mean ± σ)	8.27 ± 0.59	7.28 ± 0.75	6.63 ± 0.95	5.77 ± 1.24
Log Omnidirectional Peak Flux (mean ± σ)	3.27 ± 0.64	2.37 ± 0.82	1.88 ± 0.78	—

Data from King [1974].

means and standard deviations of the distributions for four energy thresholds are shown in Table 6-6.

6.3.2.2 Solar Electron Events. The data base for solar electron events begins with their identification in 1965. Since it is difficult to measure electrons in a high flux of penetrating protons, it was not until 1965 that the detector technology used on spacecraft was capable of uniquely distinguishing between electrons and protons. Solar electrons are present in all major solar particle events and were probably present, but not identified, in major events prior to 1965.

Solar electron events are characteristically separated into two groups: low energy solar electrons (energy ranges in the 10s of KeV) and high energy electrons (energies in the MeV range). (Since the rest mass energy of an electron is 0.511 MeV, electrons with kinetic energy in the MeV range are relativistic, and their velocity is nearly the speed of light).

Low energy electrons are emitted by many solar flares (even small ones), and there is a very good correlation between Type III radio bursts and the measurement of low energy solar electrons for "favorably" located solar flares.

Table 6-7. Average abundances relative to oxygen of energetic particle populations in the interplanetary medium.

	Solar Flare Particle Events			Solar Material	
Element	Normal (1–20 MeV)	Iron-Rich (1–5 MeV)	Corotating Particle Streams (1–10 MeV)	Corona	Photosphere
H	4600	300	2800	1780	1445
He	70	40	170	150	91*
Li	~0.0005				$\sim 1.4 \cdot 10^{-8}$
Be	<0.0007				$\sim 2 \cdot 10^{-8}$
B	<0.0007				$< 1.8 \cdot 10^{-8}$
C	0.54	0.23	1.05	1.0	0.6
N	0.13			0.2	0.126
O	≡1	≡1	≡1	≡1	≡1
F	<0.002				
Ne	0.16	0.39	0.2	0.063	0.054
Na	0.016			0.005	0.0028
Mg	0.18	0.54	0.13	0.079	0.050
Al	0.016			0.005	0.0048
Si	0.13	0.44	0.087	0.079	0.065
P	<0.002			0.0005	0.0005
S	0.026	0.33	0.06	0.0251	0.023
Ar	~0.004			0.01	0.0015
Ca	0.012			0.0045	0.0032
Fe	0.15	1.3	0.095	0.093	0.05

Data from Gloekler [1979].
*Note: The photosphere He abundance is not accurately measured and there is a large variance between the results of different measurement methods.

The frequency of the low energy solar electron events is highly correlated with solar flare frequency throughout the solar sunspot cycle. The location of the solar flare is important since low energy solar electron event detection at the earth is generally limited to heliolongitudes within ± 90° of a position about 50° West heliographic longitude.

High energy solar electron events have a distinctly different time profile from the low energy solar electron events. The high energy solar electron event profile is similar to the time-intensity profile of the 90 to 100 MeV protons. The high energy solar electrons characteristically arrive at 1 AU after the observation of the low energy solar electrons emitted from the same flare. See Simnett [1974] for a detailed study of this phenomena.

There is a special class of solar electron events called "scatter free" events. These events are very impulsive, with short interplanetary propagation times, and short rise and decay times. The data indicate that the solar electrons in these events undergo very little scattering in the interplanetary medium between the sun and the earth. The scatter free events have an upper energy limit of about 1 MeV, and detection at the earth is restricted to a relatively narrow solar flare source region about ± 30° from the Archimedean spiral path from the sun to the earth. See Section 6.3.4 for a discussion of the most favorable propagation path between the sun and the earth.

6.3.3 Elemental Composition of Solar Particle Events

Average values of the elemental abundances of ≥ 1 MeV/nucleon solar particles in relatively large solar flare events (peak intensities exceeding ~ 100 protons $cm^{-2}s^{-1}$ $sr^{-1}MeV^{-1}$) with a "normal" composition are given in Table 6-7 and shown in Figure 6-28 as solid bars, open rectangles (element groups) and solid triangles (upper limits). The abundances relative to oxygen of the individual elements or element groups are derived from a number of individual flare particle events. There is signifiant variability in the composition of normal flare particle events, not only from one event to the next but sometimes during a given event. The vertical extent of the solid bars and open rectangles indicates the degree of variability in the elemental composition. For the large events, variations in the abundances from flare to flare, and with time during single flares, give no indication that physical mechanisms preferentially accelerate any particular species over the energy range of observations. Systematic changes in the elemental composition have been observed during individual solar particle events and in successive flares from the same active region. In addition to the velocity dispersion there is a charge-to-mass dependent dispersion in the time-to-maximum for elements having equal velocities.

Despite these variabilities the basic composition of solar flare particles is similar to the composition of the solar

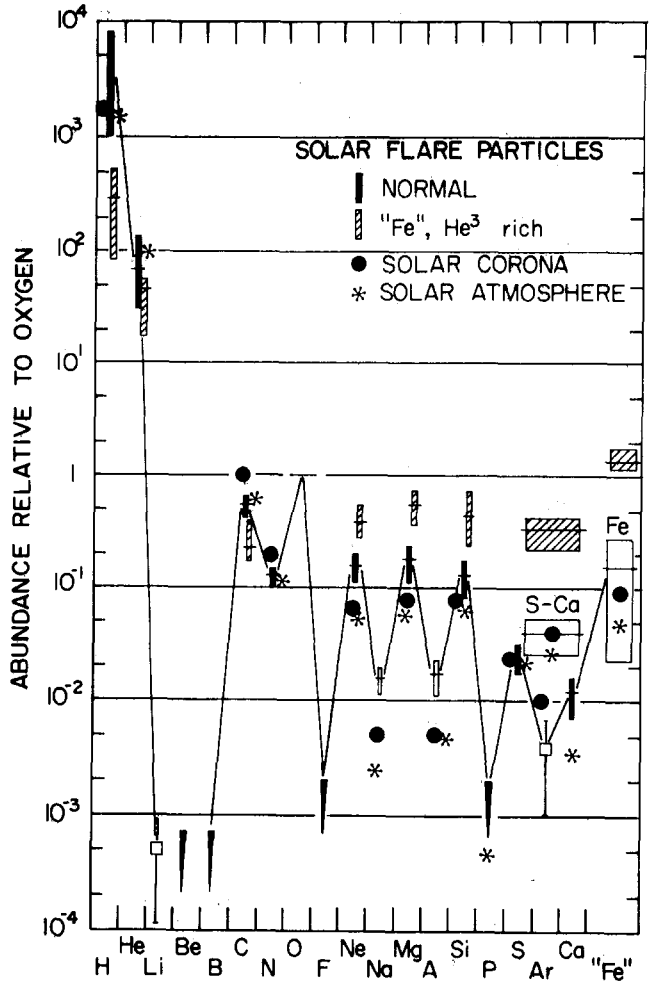

Figure 6-28. Abundances of elements and element groups normalized to oxygen in the solar corona (filled circles), solar atmosphere or photosphere (stars) and in solar flare particle events. The abundances for relatively large (peak intensities ≥~100 protons cm^{-2} s^{-1} sr^{-1} MeV^{-1}) flare particle events with a normal composition are indicated by solid vertical bars, solid triangles (upper limits), open squares (single measurement with error bars) and open rectangles (element groups). The composition for "Fe"-rich (also ^{3}He-rich) solar flare particle events is indicated by cross hatched bars and rectangles and is based on abundance measurements in the 1 to 4.6 MeV/nucleon range. The vertical extent of the bars for H, He, C, N, Ne, Mg, Si, S-Ca, and Fe in both the normal and Fe-rich events indicates the degree of variability in the composition between different solar flare particle events [Gloeckler, 1979].

corona and photosphere whose abundances are also given in Table 6-7. There is overall agreement in the abundances of He, C, N, and S through Fe; the elements Li, Be, B, F, and P are rare, and the odd Z (Z is the atomic number) elements N, F, Na, Al, and P are far less abundant than their even Z neighbors. The energetic solar particle composition seems to be consistently enriched in the elements Ne to Si, and the solar flare C/O ratio, although consistent with the solar photospheric abundance, is lower than the currently acceptable coronal abundance values. At this time

little is known about elements heavier than Fe except that their abundances are very low.

The elemental composition of the solar particle flux is basically similar for small, medium and large events; there is, however, a tendency for the He/O ratio to be somewhat larger (~ 70 to 90) for the small and medium events than the corresponding ratio for the large solar particle events [Gloeckler, 1979].

Our knowledge of the isotropic composition of solar flare particles is at this time rather limited and generally confined to the lighter elements. Typical values of the H and He isotropic ratios in the energy range of ~ 1 to 10 MeV/nucleon averaged over a number of solar flare particle events are $^2H/^1H = 7(+10, -6) \cdot 10^{-6}$, $^3H/^1H \sim 3 \cdot 10^{-6}$ and $^3H/^4H \sim (9 \pm 4) \cdot 10^{-3}$. The isotropic abundances of solar flare Ne in the energy range from 11 to 60 MeV/nucleon have recently been reported to be $^{20}Ne/^{22}Ne = 7.6 \pm 2$. This value is distinctly lower than the comparable and well established solar wind ratio of 13.1 ± 0.6. The low abundances of the carbon, oxygen, and neon isotopes ($^{13}C/C \sim 10^{-2}$, $^{17}O/O < 3 \cdot 10^{-3}$, $^{18}O/O \sim 2 \cdot 10^{-3}$, $^{21}Ne/Ne < 10^{-2}$) indicate that element production by nuclear spallation reactions in the solar atmosphere is not significant.

6.3.3.1 Charged States of Solar Particles. Direct and indirect determinations of the ionization states of solar particles indicate incomplete stripping of the heavy ions over an extended energy range up to at least ~ 5-10 MeV/nucleon. At high energies (≳10 MeV/nucleon), the ionic component of solar particle events seems to be completely stripped of electrons. Direct measurements have shown that, in general, the charge states of C, O and Fe below 1 Mev/charge in energetic solar particle events are (a) consistent with the ionization states of these elements in the solar wind (charge states of 6, 6 and 12 for C, O and Fe respectively), (b) do not vary substantially from event to event, and (c) remain constant over the energy range of the measurements of ~ 50 to 1000 keV/charge. A number of indirect determinations of charge states of Fe at higher energies (~ 1 to 10 MeV/nucleon) also indicate partial ionization.

6.3.3.2 Corotating Energetic Particle Streams. Corotating energetic particle events are modest increases in the intensity of protons and α -particles in the range of < 1 to ~ 20 MeV/nucleon, that persist for three to six days and often reappear a number of times at ~ 27-day intervals. These corotating or 27-day recurrent increases are not associated with solar flares and do not exhibit the velocity dispersion often observed at the onset of solar flare particle events but are correlated with high-speed solar wind streams and interplanetary magnetic field structures corotating with the sun. Measurements of radial gradients and particle anisotropies in corotating events combined with the temporal-spatial correlations observed at ~ 4 to 5 AU between the ~ 1 MeV/nucleon corotating particles and the magnetic field and plasma turbulence in the corotating interaction region (CIR) provide evidence for the continuous acceleration of particles in the interplanetary medium between ~ 2 and 5 AU. The acceleration mechanisms proposed most frequently include both statistical processes resulting from magnetic and plasma turbulences that are generated when high and low speed solar wind streams collide in the corotating interaction region, and acceleration at the forward and reverse shocks which bound the corotating interaction region.

Of the possible sources for the corotating energetic particles, the most likely candidates are either the high-energy tail of the solar wind or a possible but so far undetected, low energy(< 200 keV/nucleon) residual particle population, presumably of solar origin.

6.3.4 Prediction of Solar Proton Events

The capability to predict a phenomenon such as a solar proton event illustrates our understanding of the processes controlling such a phenomenon. Solar protons are accelerated in solar active regions during solar flare events. The x-ray, radio and optical emissions during the solar flare event are the indicators that particle acceleration is occurring. The "U-shaped" spectral signature in the radio emission peak power spectrum [Castelli et al., 1967; Castelli and Guidice, 1976] can be interpreted as the indicator that solar protons are being released from the solar active region (see Chapter 11). After the energetic particles are released from the accelerating region, they will travel through the solar corona and some will propagate outwards along the interplanetary magnetic field lines to the position of the earth. A computerized code to predict solar proton intensities at the earth after the occurrence of a specific solar flare has been developed by Smart and Shea [1979].

6.3.4.1 Propagation of Solar Particles. The propagation of solar protons from the flare site to the earth can be separated into two distinct phases. The first phase is diffusion from the flare site through the solar corona to the "foot" of the Archimedean sprial path formed by the interplanetary magnetic field line between the sun and the earth. The second phase is the propagation in the interplanetary medium from the sun to the earth along the interplanetary magnetic field lines. Figure 6-29 provides an illustration of the propagation concepts.

Propagation in the Solar Corona. The angular distance the solar particles travel in the solar corona from the presumed source (that is, the solar flare site) to the foot of the Archimedean spiral path from the sun to the earth is designated by the symbol θ in Figure 6-29. In a heliographic coordinate system the solar flare will have coordinates defined as solar latitude λ_F and heliocentric longitude ϕ_F, where ϕ_F is positive west of central meridian, and ϕ_F is negative east of central meridian. If the "foot" of the Ar-

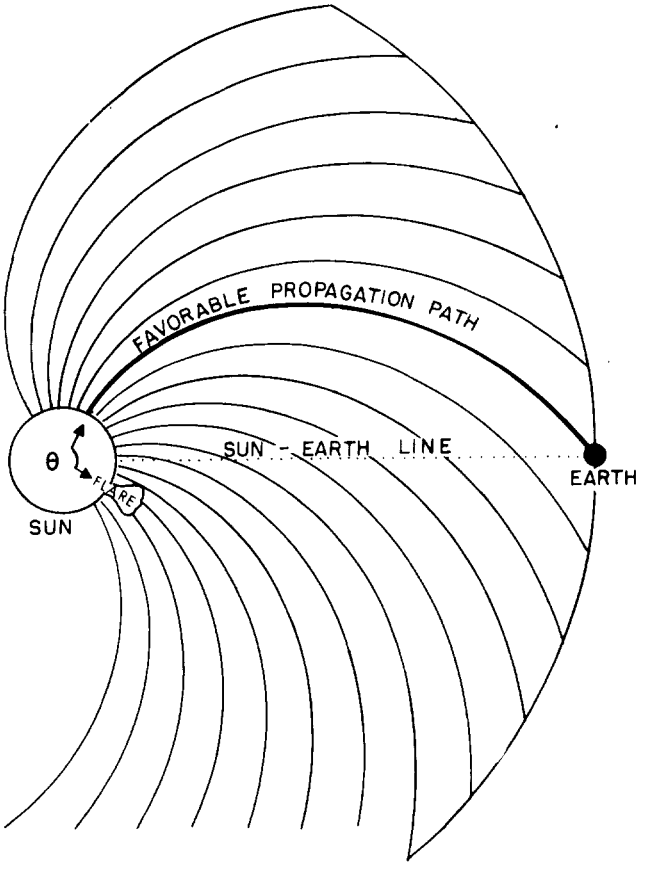

Figure 6-29. Illustration of the concept of solar particle propagation from the sun to the earth. The coronal propagation distance θ is illustrated by the heavy arc on the sun. Interplanetary propagation proceeds along the Archimedean spiral path from the sun to the earth.

chimedean spiral is at heliocentric longitude ϕ_A, then the heliocentric longitudinal distance from the flare site to the "foot" of the Archimedean spiral will be $|\phi_A - \phi_F|$. It is assumed that coronal propagation is a function of θ, and from diffusion theory, it is expected to be proportional to θ^2 [Wibberenz, 1974].

As a result of diffusion in the solar corona and the inherent assumption that some stochastic processes are operating, there will be a solar particle gradient existing in the solar corona such that the proton intensity decreases as a function of distance from the flare site. The observational evidence shows that the gradient may vary from case to case. An observer at one astronomical unit who is connected via the interplanetary magnetic field to the heliographic position of the flaring region would observe the maximum possible particle intensity. An observer whose interplanetary magnetic field connection is at a distance of θ from the flaring location would observe a reduced intensity. Observational data suggest an average gradient may be about one order of magnitude per radian of heliocentric distance.

Propagation in the Interplanetary Medium. After the energetic solar particles propagate through the solar corona

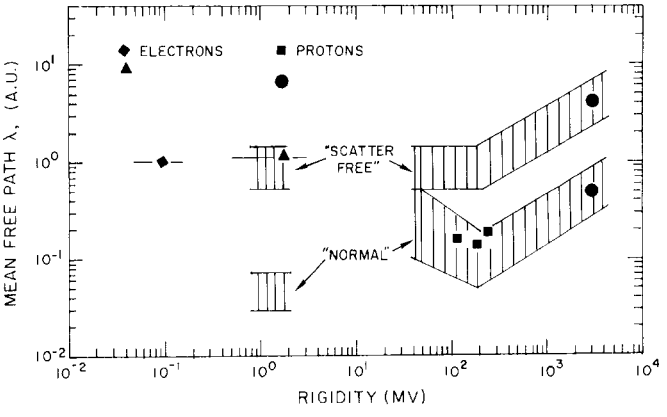

Figure 6-30. Interplanetary mean free path $\lambda_\parallel$ as a function of charged particle rigidity. These data have been derived from an analysis of many solar particle events. The shaded areas indicate the range of "scatter free" (upper region) and "normal" (lower region) propagation in the interplanetary medium.

and are released into the interplanetary medium, they propagate along the interplanetary magnetic field lines. (See Chapter 3 for a detailed description of the solar wind.)

The spiral structure of the interplanetary magnetic field shown in Figure 6-29 is highly idealized. On a microscale there are many irregularities in the interplanetary medium. The energetic solar particles propagating through the interplanetary medium will undergo random scattering and the same general theory described in Section 6.2.2.1 applies. The mean free path between scattering centers is quite variable, depending on both the particle energy and the amount of turbulance in the interplanetary medium. A summary of the general range of mean free paths determined from a number of solar particle events is illustated in Figure 6-30.

During the sun to earth phase of their propagation, the MeV solar particles appear to have an average mean free path length of the order of 0.1 to 0.3 AU; consequently, over the 1 AU radial distance, diffusion perpendicular to the interplanetary magnetic field line is negligible. The energetic particles travel essentially along the interplanetary magnetic field lines with a velocity that is a function of the particle energy. The minimum propagation delay will be for particles that essentially travel along the interplanetary magnetic field lines with miminal scattering, so for "scatter free" onsets the propagation time from the sun to the earth will be the distance traveled along the Archimedean spiral path divided by the particle velocity.

Some scattering certainly occurs in the interplanetary medium, and to determine the time of maximum intensity, diffusion theory is applicable. Almost all theories involving solar particle transport in the interplanetary medium show that the time of maximum is proportional to the square of the distance traveled. The distance travelled can be obtained by integrating along the Archimedean spiral path. Normalized to the earth's orbit at 1 AU, in a heliographic coordinate system, the Archimedean spiral path length, D, is

$$D = 1/2\left[\sqrt{\phi_A^2 + 1} + \frac{\ln\phi_A + \sqrt{\phi_A^2 + 1}}{\phi_A}\right] \quad (6.19)$$

where ϕ_A is the heliographic longitude of the "foot point" where the Archimedean spiral path to the earth connects to the sun. If the solar wind plasma carries "frozen in" magnetic fields, then the heliographic longitude of the "foot point" of the interplanetary magnetic field line that extends from the sun to the earth is given by $\phi_A = (\omega_s r)/V_{sw}$, where ω_s is the solar synodic rotation rate (13.3 degrees/day), r is 1 AU, and V_{sw} is the velocity of the solar wind in km/s at the earth. If the Archimedean spiral equation in the polar form is normalized to 1 AU, then $\phi_A = 404/V_{sw}$ where 404 is the nominal solar wind velocity when the solar rotation is equal to one radian during the time it takes the plasma element to travel 1 AU.

The velocity of a proton is given by

$$\beta = \left[1 - \frac{1}{(E/m_oc^2 + 1)^2}\right]^{1/2} \quad (6.20)$$

where E is the kinetic energy of the particle in MeV, β is the velocity of the particle compared with the velocity of light, and the rest energy of the proton m_oc^2 has the value of 938.232 MeV. (Note: $\beta = V/c$.)

The minimum time in hours required for a proton to propagate along the Archimedean spiral path from the sun to the earth with zero pitch angle and no scattering is 0.133 D/β.

6.3.4.2 Particle Increase Onset Time. The delay time from the solar flare until the onset of the particle increase at the earth is the combination of the coronal propagation time and the time for the particles to propagate from the sun to the earth along the interplanetary magnetic field lines.

The distribution of onset times expected for 30 MeV protons for nominal solar wind speeds is shown in Figure 6-31. In this figure the heavy solid line has the functional form of $4\theta^2$; the data points shown on the figure are taken from Barouch et al. [1971] and indicate typical variations that may be expected. The minimum in the figure corresponds to a flare at the heliographic longitude of the "foot point" of the nominal Archimedean spiral path between the sun and the earth (57.2° West of central meridian). The initial onset will be for the fastest (highest energy) protons. The onset time is given by

$$T_d \text{ (in hours)} = \frac{0.133\ D}{\beta} + 4\theta^2, \quad (6.21)$$

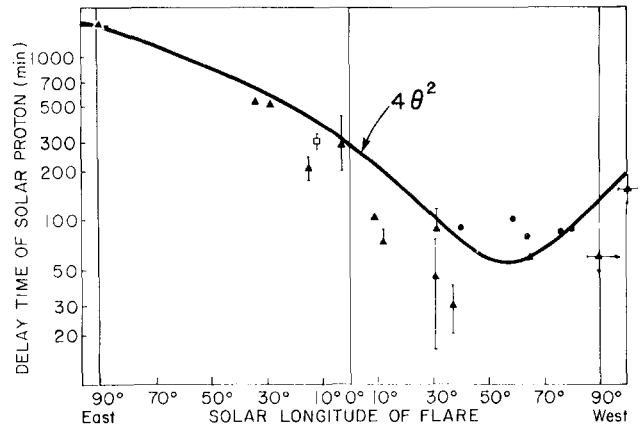

Figure 6-31. Distribution of observed onset times of 30 MeV protons as a function of solar longitude. The data points are the measurements of Barouch et al. [1971].

where D is the distance along the length of the Archimedean spiral from the sun to the earth and β is the proton velocity. This calculation can be repeated for each proton energy (velocity) desired to obtain the velocity dispersion of the predicted onset times as a function of energy.

6.3.4.3 Time of Maximum Particle Intensity. The distribution of the time of the maximum of 20 to 80 MeV protons observed at the earth for a number of proton events [Van Hollebeke et al., 1975] as a function of solar longitude is illustrated in Figure 6-32 where the heavy solid line has the functional form of $8\theta^2$. The minimum in the curve corresponds to a flare at the "foot point" of the Archimedean spiral path between the earth and the sun which would be about 57.2° for a nominal solar wind of 404 km/s.

The time of maximum can be computed by assuming the particles have an average bulk velocity that is about half

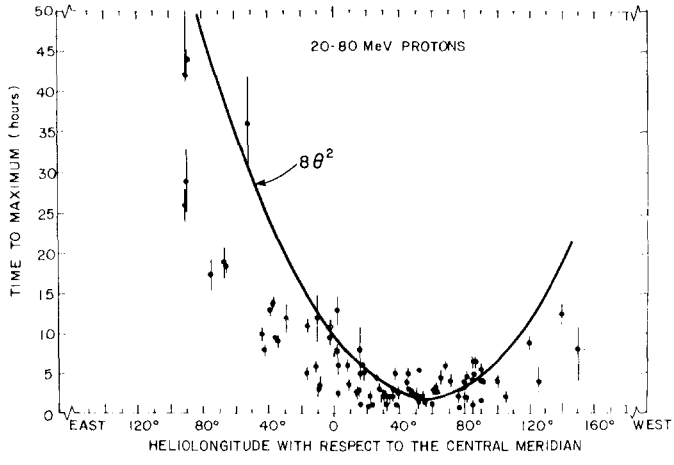

Figure 6-32. Distribution of observed times of maximum of 20 to 80 MeV protons as a function of solar longitude. The data points are the measurements of Van Hollebeke et al. [1975].

of the particle speed that would be computed from the particle energy. Most theoretical models set the time of maximum proportional to the square of the distance traveled along the magnetic field line from the sun. The time of maximum intensity is computed by

$$T_m \text{ (in hours)} = 2.0\frac{0.133\ D^2}{\beta} + 8\theta^2. \qquad (6.22)$$

6.3.4.4 Magnitude of Maximum Intensity. The maximum intensity is predicted by converting an electromagnetic emission parameter (usually radio flux or x-ray flux) to a proton flux. Many different algorithms can be used but currently the best predictors are the relationships between integrated radio flux and peak proton flux. The maximum particle intensity is expected to be along the Archimedean spiral path from the flare. The maximum particle intensity expected at the earth is derived by attenuating the flux through the coronal gradient over the heliocentric distance in the corona between the flare position and the solar equatorial longitude of the "foot point" of the Archimedean spiral path from the sun to the earth.

6.3.4.5 Proton Event Decay. The decaying portion of a solar particle event is normally exponential in character with a nominal time constant for the flux to decay by a factor of 1/e although there is a slight energy dependence, and there can be a large variability between events.

The decaying portion of the event can be modeled after the principles of diffusive particle transport in the interplanetary medium. One such method is collimated convection [Roelof, 1973]. This results in a 1/e decay constant of

$$T_d \text{ (in hours)} = \frac{3D}{4V_{sw}(|\gamma| + 1)\ 3600}, \qquad (6.23)$$

where T_d is the 1/e decay constant, D is the distance along the Archimedean spiral path, V_{sw} is the solar wind velocity, and γ is the differential energy spectral exponent.

Effect of Coronal Gradient on Apparent Decay Rate. The assumption that there is a particle gradient in the corona combined with the solar rotation, results in a decay rate at the earth that is dependent on the solar flare location. After the particle flux maximum, the flux along the interplanetary magnetic field lines can be considered as a corotating structure being convected out into space. If the particle source is a flare on the eastern hemisphere or near central meridian of the sun, the particle coronal longitudinal flux gradient rotates toward the "foot point" of the Archimedean spiral from the sun to the earth; thus the apparent decay rate will be slower than the radial convection rate out from the sun. If the particle source rotates away from the "foot point," as is the case for flares that occur on the extreme western hemisphere of the sun, then the solar rotation and the coronal particle longitudinal gradient will combine to increase the flux decay rate at the earth.

6.3.4.6 Differential Energy Spectra. The slope of the differential energy spectrum of solar proton events observed at the earth is summarized by Van Hollebeke et al. [1975] and shown in Figure 6-33. Assuming that the hardest spectra (the minimum in the solid curve of Figure 6-33) should be along the interplanetary magnetic field lines leading away from the flare site, the average spectral slope is observed to vary as

$$\gamma_f = -2.7\left(1.0 + \frac{\theta}{2}\right). \qquad (6.24)$$

6.3.4.7 Prediction of Polar Cap Absorption. It is possible to convert predicted proton flux to prediction of the profile of the riometer absorption in the polar ionosphere. It has been shown that riometer absorption is proportional to the square root of the intergal proton flux above some specified energy. A convenient relationship is $J_{(>10)} = 10A^2$, where $J_{(>10)}$ is the flux of protons with energy greater then 10 MeV and A is the absorption in decibels for a 30 MHz riometer. The relationships developed by Sellers et al. [1977] are simple equations that are relatively independent of the slope of the solar proton energy spectrum. These authors selected the integral proton flux greater than 5.2 MeV and 2.2 MeV to be a good predictor of the riometer absorption in the sunlit polar ionosphere and the night time polar ionosphere respectively. These equations are

$$A \text{ (day)} = 0.6[J_{(>5.2)}]^{1/2} \qquad (6.25)$$

$$A \text{ (night)} = 0.25[J_{(>2.2)}]^{1/2}. \qquad (6.26)$$

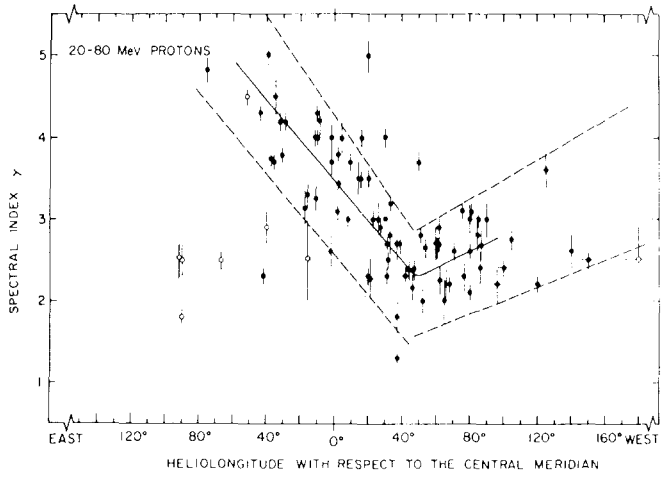

Figure 6-33. Variation of the absolute value of spectral index γ in the 20–80 MeV range as a function of the heliolongitude. The dashed contour lines enclose 92% of the "normal" events. The solid line is a least squares fit that can be represented by 2.7[1 + θ/2].

CHAPTER 6

REFERENCES

Adams, J.H. Jr., R. Silverberg, and C.H. Tsao, "Cosmic Ray Effects on Microelectronics, Part I: The Near Earth Particle Environment," NRL Rept. 4056, Naval Research Laboratory, Washington, D.C. 1981.

Akiniyan, S.T., G.A. Bazilevskaya, V.N. Ishkov, et al., *Catalog of Solar Proton Events 1970—1979*, Institut Zemnogo Magnetizma, Ionosfery I Rasprostraneniya Radiovoln (Institute of Earth Magnetism, Ionosphere and Radiowave Propagation), Academy of Science, USSR, 1983.

Allkover, O.C. and P.K.F. Grieder, *Cosmic Rays on Earth, Physics Data 25-1*, Fachinformationszentrum Energie, Physik, Mathematik, Gmbh, Karlsruhe, Germany, 1984.

Armstrong, T.W., K.C. Chandler, and J. Barish, "Calculations of Neutron Flux Spectra Induced in the Earth's Atmosphere by Galactic Cosmic Rays," *J. Geophys. Res.*, **78:** 2715, 1973.

Barouch, E., M. Gros and P. Masse, "The Solar Longitude Dependence of Proton Event Decay," *Sol. Phys.*, **19:** 483, 1971.

Cameron, A.G.W., "Elementary and nuclidic abundances in the solar system," in *Essays in Nuclear Astrophysics*, edited by C.A. Barnes, D.D. Clayton, and D.N. Schramm, Cambridge University Press, Cambridge, England, 1981.

Castelli, J.P., and D.A. Guidice, "Impact of Current Solar Radio Patrol Observations," *Vistas in Astron.*, **19:** 355, 1976.

Castelli, J.P., J. Aarons, and G.A. Michael, "Flux Density Measurements of Radio Bursts of Proton-Producing and Nonproton Flares," *J. Geophys. Res.*, **72:** 5491, 1967.

Chupp, E.L., D.J. Forrest, J.M. Ryan, J. Heslin, C. Reppin, K. Pinkau, G. Kanbach, E. Rieger, and G.H. Share, "A Direct Observation of Solar Neutrons Following the 0188 UT Flare on 1980 June 21," *Astrophys. J. Lett.*, **263:** L95–L99, 1982.

Claflin, E.S. and R.S. White, "A Study of Equatorial Inner Belt Protons from 2 to 200 MeV," *J. Geophys. Res.*, **79:** 959, 1974.

Dodson, H.W., E.R. Hedeman, R.W. Kreplin, M.J. Martres, V.N. Obridko, M.A. Shea, D.F. Smart, and H. Tanaka, *Catalog of Solar Particle Events 1955–1969*, Vol. 49 of the Astrophysics and Space Science Library, edited by Z. Svestka and P. Simon, D. Reidel, Dordrecht, Holland, 1975.

Ely, J.T.A., "Atmospheric Depth and Effective Solid Angle for Radiation Penetrating the Atmosphere," *Geophysics Research Papers No. 74* (AFCRL 62-260), Air Force Cambridge Research Laboratories, 1962.

Eraker, J.H. and J.A. Simpson, "Origins of the Low Energy Relativistic Interplanetary Electrons," Proceedings of the 17th International Cosmic Ray Conference Paris 1981 *Conference Papers*, **3:** 279, Centre d'Etudes Nucleaires, Saclay, France, 1981.

Fanselow, J.L. and E.C. Stone, "Geomagnetic Cutoffs for Cosmic-Ray Protons for Seven Energy Intervals between 1.2 and 39 MeV," *J. Geophys. Res.*, **77:** 3999, 1972.

Forman, M.A. and O.A. Schaeffer, "Cosmic Ray Intensity Over Long Time Scales," *Rev. Geophys. and Sp. Phys.*, **17:** 552, 1979.

Garcia-Munoz, M., G.M. Mason, and J.A. Simpson. "The Anomalous He component in the Cosmic Ray Spectra of $\leq$ 50 MeV per Z Nucleon During 1972–1974," *Astrophys. J.*, **202:** 265, 1975.

Gleeson, L.J. and W.I. Axford, "Cosmic Rays in the Interplanetary Medium," *Astrophys. J.*, **149:** L115, 1967.

Gleeson, L.J. and W.I. Axford, "Solar Modulation of Galactic Cosmic Rays," *Astrophys. J.*, **154:** 1011, 1968.

Gloeckler, G. "Composition of Energetic Particle Populations in Interplanetary Space," *Rev. Geophys. Space Phys.*, **17:** 569, 1979.

Haffner, J.W., "Radiation and Shielding in Space," *Nuclear Science and Technology 4*, Academic Press, New York, 1967.

Hess, W.N., H.W. Patterson, R. Wallace, and E.L. Chupp, "Cosmic-ray Neutron Energy Spectrum," *Phys. Rev.*, **116:** 445, 1959.

Israel, M.H., "Cosmic Ray Electrons Between 12 MeV and 1 Gev in 1967," *J. Geophys. Res.*, **74:** 4701, 1969.

King, J.H., "Solar Proton Fluences for 1977–1983 Space Missions," *J. Spacecraft and Rockets*, **11:** 401, 1974.

Kurnosova, L.V., "Charged Particle Flux at 200 to 300 km above the Earth" in *Cosmic Rays in the Stratosphere and Near Space*, edited by N.G. Basov, Lebedev, Trudy 88, Proceedings of the P.N. Lebedev Institute, **88:** 137, 1976. Engl transl Consultants Bureau, New York, 1978.

Kykler, G.C. and A.R. Liboff, "Absolute Cosmic Ray Ionization Measurement in a 900-Liter Chamber," *J. Geophys. Res.*, **82:** 5539, 1978.

Levy, E.H., S.P. Duggal, and M.A. Pomerantz, "Adiabatic Fermi Acceleration of Energetic Particles Between Converging Interplanetary Shock Waves," *J. Geophys. Res.*, **81:** 51, 1976.

Lezniak, J.A. and W.R. Webber, "The Charge Composition and Energy Spectra of Cosmic-Ray Nuclei from 3000 MeV per Nucleon to 50 GeV Per Nucleon," *Astrophys. J.*, **223:** 1978.

Light, E.S., M. Merker, H.J. Verschell, R.B. Mendell, and S.A. Korff, "Time Dependent World Wide Distribution of Atmospheric Neutrons and of Their Products, 2. Calculations," *J. Geophys. Res.*, **78:** 2741, 1973.

Lingenfelter, R.E., "The Cosmic Ray Neutron Leakage Flux," *J. Geophys. Res.*, **68:** 5633, 1963.

McCracken, K.G., U.R. Rao, B.C. Fowler, M.A. Shea, and D.F. Smart, "Cosmic Ray Tables," *IQSY Instruction Manual No. 10*, IQSY Committee, London, 1965.

McCracken, K.G., U.R. Rao, B.C. Fowler, M.A. Shea, and D.F. Smart, "Cosmic Rays (Asymptotic Directions, etc)" in Chapter 14 of *Annals of the IQSY, Vol. 1*, (Geophysical Measurements: Techniques, Observational Schedules and Treatment of Data) edited by C.M. Minnis, 198, MIT Press, Cambridge, Mass., 1968.

McDonald, F.R., ed., *Solar Proton Manual*, National Aeronautics and Space Administration Technical Report, NASA TR-R-169, 1963.

McIlwain, C.E., "Coordinates for Mapping the Distribution of Magnetically Trapped Particles," *J. Geophys. Res.*, **66:** 3681, 1961.

Mewaldt, R.A., "The Elemental and Isotopic Composition of Galactic Cosmic Rays," Proceedings of the 17th International Cosmic Ray Conference, *Conference Papers,* **13:** 49, Centre d'Etudes Nucleaires, Saclay, France, 1981.

Murakami, K., K. Nagashima, S. Sagisaka, Y. Mishima, and A. Inoue, "Response Functions for Cosmic-Ray Muons at Various Depths Underground," *Nuovo Cimento, 2C:* 635, 1979.

Neher, H.V., "Cosmic Ray Particles that Changed from 1954 to 1958 and 1965," *J. Geophys. Res.*, **72:** 1527, 1967.

Neher, H.V., "Cosmic Rays at High Latitudes and Altitudes Covering Four Solar Maxima," *J. Geophys. Res.*, **76:** 1637, 1971.

O'Brian, K., "Calculated Cosmic Ray Ionization in the Lower Atmosphere," *J. Geophys. Res.*, **75:** 4357, 1970.

O'Brian, K., "Secular Variations in the Production of Cosmogenetic Isotopes in the Earth's Atmosphere," *J. Geophys. Res.*, **84:**423, 1979.

Peddie, N.W., "International Geomagnetic Reference Field: The Third Generation," *J. Geomag. Geoelectr.*, **34:** 309, 1982.

Roelof, E.C., "New Aspects of Interplanetary Propagation Revealed by 0.3 MeV Solar Proton Events in 1967," in *Solar-Terrestrial Relations.*, 411, University of Calgary, Canada, 1973.

Rossi, B., *High Energy Particles,* Prentice-Hall, New York, 1952.

Rossi, B., *Cosmic Rays,* McGraw Hill, New York, 1964.

Sellers, B., F.A. Hanser, M.A. Stroscio, and G.K. Yates, "The Night and Day Relationships betweeen Polar Cap Riometer Absorption and Solar Protons," *Radio Sci.*, **12:** 779, 1977.

Seltzer, S. "SHIELDOSE: A computer code for Space-shielding Radiation Dose Calculations," NBS Technical Note 1116, National Bureau of Standards, U.S. Department of Commerce, Washington, D.C., May 1980.

Shea, M.A. and D.F. Smart, "A Five by Fifteen Degree World Grid of Calculated Cosmic-Ray Vertical Cutoff Rigidities for 1965 and 1975," 14th International Cosmic Ray Conference, *Conference Papers*, **4:** 1298–1303, 1975.

Shea, M.A., and D.F. Smart, "A World Grid of Calculated Cosmic Ray Vertical Cutoff Rigidities for 1980.0," 18th International Cosmic Ray Conference, *Conference Papers,* **3:** 415, 1983.

Shea, M.A., D.F. Smart, and John R. McCall, "A Five Degree by Fifteen Degree World Grid of Trajectory-Determined Vertical Cutoff Rigidities," *Can. J. Phys.*, **46:** S1098, 1968.

Simnett, G.M., "Relativistic Electron Events in Interplanetary Space," *Space Sci. Revs.*, **16:** 257, 1974.

Smart, D.F. and M.A. Shea, "Solar Proton Event Classification System," *Sol. Phys.*, **16:** 484, 1971.

Smart, D.F. and M.A. Shea, "PPS76 - A Computerized "Event Mode" Solar Proton Forecasting Technique," *Solar-Terrestrial Predictions Proceedings, Vol. 1:* Prediction Group Reports, edited by R.F. Donnelly, Environment Research Laboratories, National Oceanic and Atmospheric Administration, U.S. Department of Commerce, Boulder, CO, 406, 1979.

Stassinopoulos, E.G., and J.H. King, "An Empirical Model of Energetic Solar Proton Fluxes with Application to Earth Orbiting Spacecraft," NASA X-601-72-487, 1972.

Stuiver, M. and P.D. Quay, "Changes in Atmospheric Carbon-14 Attributed to a Variable Sun," *Science*, **207:** 11, 1980.

Van Hollebeke, M.A.I., L.S. Ma Sung, and F.B. McDonald, "The Variation of Solar Proton Energy Spectra and Size Distribution with Heliolongitude," *Sol. Phys.*, **41:** 189, 1975.

Wenzel, K.-P., E.C. Stone, and R.E. Vogt, "Splash Albedo Protons Between 4 and 315 MeV at High and Low Geomagnetic Latitudes," *J. Geophys. Res.*, **80:** 358, 1975.

West, G.S. Jr., S.J. Wright, and H.C. Euler, (eds.), "Space and Planetary Environment Criteria Guidelines for use in Space Vehicle Developments," NASA-TM-78119, 1977.

Wibberenz, G., "Interplanetary Magnetic Fields and the Propagation of Cosmic Rays," *J. Geophys.*, **40:** 667, 1974.